JOURNAL OF GEOPHYSICAL RESEARCH, VOL. 106, NO. B4, PAGES 6569–6587, APRIL 10, 2001

# Tomographic imaging of the lowermost mantle with differential times of refracted and diffracted core phases (*PKP*, $P_{\mathrm{diff}}$)

Hrafnkell Kárason and Rob D. van der Hilst
Department of Earth, Atmospheric and Planetary Sciences, Massachusetts Institute of Technology
Cambridge, Massachusetts

**Abstract.** The mapping of variations in $P$ wave speed in the deep mantle is restricted by the uneven sampling of $P$ waves, in particular beneath the Southern Hemisphere. To enhance data coverage, we augmented the ~1.6 million summary rays of $P$, $pP$, and $pwP$ that we used in previous studies with differential travel times of diffracted and refracted core phases. For the core-refracted differential travel time residuals ($PKP_{\mathrm{AB}}$-$PKP_{\mathrm{DF}}$ and $PKP_{\mathrm{AB}}$-$PKP_{\mathrm{BC}}$) we used 1383 cross-correlated digital waveforms as well as ~27,000 routinely processed bulletin data. We used the waveform data to define quality criteria for the selection and reduction of the bulletin $PKP$ data. For $PKP_{\mathrm{DF}}$-$P_{\mathrm{diff}}$ we only considered 543 records derived from waveform cross correlation. No $PcP$ data were used in this study. We used optical ray theory to calculate the ray paths associated with the $P$, $pP$, $pwP$, and $PKP$ data, which are measured at 1 Hz. However, to account for the large Fresnel zones of the low-frequency (~50 mHz) $PKP_{\mathrm{DF}}$-$P_{\mathrm{diff}}$ data we estimated the three-dimensional shape of the Fréchet sensitivity kernels from kernels calculated by normal mode summation. The use of these kernels allows us to properly distribute the sensitivity for a given seismic phase over a large mantle volume while allowing the high-frequency data to constrain small-scale structure. The differential times are relatively insensitive to source mislocation and to structure in the shallow mantle beneath source and receivers, and they have previously been interpreted exclusively in terms of lateral structure directly above the core mantle boundary (CMB). However, images thus obtained can be contaminated by effects of small scale structure elsewhere in the mantle. Here, we do not make a priori assumptions about the mantle source of anomalous time differentials. From test inversions we conclude that (both upper and lower) mantle structures that are poorly resolved by $P$ data can be mapped into the core along $PKP$ paths but that the effect of outer core structures, if any, on the mantle model is small. Compared to the inversion of the $P$, $pP$, and $pwP$ alone, the inclusion of the $PKP_{\mathrm{AB}}$-$PKP_{\mathrm{DF}}$ and $PKP_{\mathrm{AB}}$-$PKP_{\mathrm{BC}}$ and $PKP_{\mathrm{DF}}$-$P_{\mathrm{diff}}$ data improves the resolution of structure beneath 2200 km depth. In particular, the joint inversion puts better constraints on the long-wavelength variations in the very deep mantle and yields an increase in the amplitude of velocity perturbations near the CMB that is in agreement with but still smaller than inferences from shear wave studies. Resolution tests indicate that in some regions the enhanced definition of structure is significant, but in most regions the improvements are subtle and structure remains poorly resolved in large regions of the mantle.

## 1. Introduction

In the last decade, continuous improvement of seismic imaging techniques, data quality, and computer power has resulted in increasingly detailed images of Earth's interior structure [*Su et al.*, 1994; *Li and Romanowicz*, 1996; *Masters et al.*, 1996; *van der Hilst et al.*, 1997; *Grand et al.*, 1997; *Vasco and Johnson*, 1998; *Bijwaard et al.*, 1998; *Kárason and van der Hilst*, 2000]. There is growing agreement on the large-scale (>4000 km) structure of the upper and lowermost mantle [*Dziewonski et al.*, 1999]. Studies based on body and surface waves have discovered high wave speed anomalies beneath the stable continents and low wave speeds beneath tectonically active regions and marginal basins and travel time tomography has revealed relatively narrow structures of higher-than-average seismic wave speed beneath convergent margins [i.e., *Grand*, 1994; *van der Hilst et al.*, 1997; *Bijwaard et al.*, 1998; *Vasco and Johnson*, 1998]. These narrow features have been interpreted as subducted slab. Recent studies suggest that some

Copyright 2001 by the American Geophysical Union.

Paper number 2000JB900380.
0148-0227/01/2000JB900380$09.00

of these slabs continue into the lower mantle, which renders unlikely convection models with two distinct layers separated by the seismic discontinuity at 660 km depth.

Statistical analysis of International Seismological Centre (ISC) residuals suggests an increase in the amplitude of long-wavelength structure in the lowermost mantle, reaching a maximum at the core-mantle-boundary (CMB) [*Gudmundsson et al.*, 1990], which is in accord with tomographic imaging that revealed relatively slow and fast propagation beneath Africa and the Pacific and in large regions beneath the Americas and eastern Asia, respectively [e.g., *Su et al.*, 1992]. Other studies reported a decreased correlation between $S$ and $P$ wave speed perturbations in the deep mantle which may in part be due to changes in bulk composition [e.g., *Robertson and Woodhouse*, 1995; *Su and Dziewonski*, 1997; *Kennett et al.*, 1998; R.L. Saltzer and R.D. van der Hilst, submitted manuscript, 2000]. These and other observations inspired *van der Hilst and Kárason* [1999] to propose the existence of compositionally distinct domains in the deep mantle, which could host heat-producing elements and certain noble gases [*Kellogg et al.*, 1999; *Albarède and van der Hilst*, 1999]. There is also evidence for small-scale structures near the base of the mantle, including ultralow-velocity zones and rapid lateral variations in anisotropy (see *Garnero* [2000] for a review), but this complexity cannot be resolved with the techniques discussed here.

Between 1000 and 2000 km depth the amplitude of the wave speed variations is small, the scatter in the pertinent data is high [*Gudmundsson et al.*, 1990], and the spectrum of heterogeneity, white, at least up to degree 12 [e.g., *Su and Dziewonski*, 1992]. Global tomography suggests the presence of deep slabs of subducted lithosphere [*van der Hilst et al.*, 1997, 1998; *Grand et al.*, 1994], but in some models a slab signature is not evident beneath $1700 \pm 300$ km depth [e.g.,*van der Hilst and Kárason*, 1999; and *Kárason and van der Hilst*, 2000). A transition from middle to lowermost mantle structure has been proposed [*Su et al.*, 1994; *van der Hilst et al.*, 1997; *Liu and Dziewonski*, 1998; *van der Hilst and Kárason*, 1999], but uncertainty remains about its existence, the depth of onset, and its impliciations for mantle flow.

While models of mantle $S$ wave speed can be constrained by body waves, long period surface waves, and observed frequency shifts of Earth's free oscillations [e.g., *Masters et al.*, 1996], global $P$ models have traditionally been derived from travel times of body wave phases that are confined to the mantle, such as $P$ [*Dziewonski et al.*, 1977; *Inoue et al.*, 1990; *Pulliam et al.*, 1993], $pP$ [*van der Hilst et al.*, 1997; *Bijwaard et al.*, 1998], or $PP$ [*Vasco et al.*, 1995a]. The spatial coverage by these phases is, however, very uneven owing to the distribution of earthquakes and stations and to the geometry of the ray paths (Figure 1a).

Large regions in the lower mantle, especially in the Southern Hemisphere, are not adequately sampled owing to the scarcity of stations. In such regions, tomographic imaging will underestimate the true amplitude of the wave speed variations or not reveal them at all. *Song and Helmberger* [1997] showed that the model by *van der Hilst et al.* [1997] explains only ~20% of the variance of observed $PKP$ travel times and concluded that the amplitudes of $P$ velocity variations in the lower mantle were underestimated by up to 1 order of magnitude. *Van der Hilst et al.* [1998] showed that the pattern (but not the magnitude) of $PKP$ differential time residuals measured by *McSweeney* [1995], mapped at the exit and entry points at the CMB, is consistent with their tomographic model. Assuming that they sense structure near the very base of the mantle, *Wysession* [1996] argued that $PKP_{\mathrm{DF}}$-$P_{\mathrm{diff}}$ differential travel time residuals require higher levels of velocity perturbations than is typically inferred from mantle tomography.

To improve sampling, Vasco and co workers [*Pulliam et al.*, 1993; *Vasco et al.* 1993, 1994, 1995a] used ISC data from a large range of seismic phases. Their most recent $P$ wave model is based on $P$, $PP$, $PKP_{\mathrm{AB}}$, $PKP_{\mathrm{BC}}$, $PKP_{\mathrm{DF}}$, and $PcP$ (absolute) travel time residuals [*Vasco and Johnson*, 1998]. The addition of core-reflected and -refracted phases enhances data coverage and improves the resolution. However, estimates or formal calculations of resolution depend on data coverage only, and it is not well known to what extend the high noise level in later arriving phases, in particular $PcP$, degrades the model.

Here, we aim to improve models of the deep mantle by using differential travel time times of core-refracted and -diffracted phases along with (absolute) travel time residuals of mantle $P$ and $pP$ waves. Instead of relying on routinely processed data we use $PKP_{\mathrm{DF}}$-$P_{\mathrm{diff}}$ data from *Wysession* [1996] and $PKP_{\mathrm{AB}}$-$PKP_{\mathrm{DF}}$ and $PKP_{\mathrm{AB}}$-$PKP_{\mathrm{BC}}$ residuals from *McSweeney* [1995] (see Figure 1a for ray geometry). These differential travel time residuals have been determined using waveform cross correlation. We also used the large number of $PKP$ times from the data set of *Engdahl et al.* [1998] to construct differential travel time residuals.

For the inclusion of the differential times in our tomographic scheme we used the approach described by *van der Hilst and Engdahl* [1991] for $pP - P$ and $PP - P$ data so that we do not need to make any a priori assumption for the localization of the source of the structural signal. Including the diffracted $P$ waves in travel time tomography for three-dimensional mantle structure is, however, not trivial because (1) it is not a ray geometrical phase (it is evanescent and dispersive so that the observed travel time and its sensitivity to structure are frequency dependent) and (2) they were measured at much longer period than both the routinely processed ($P$, $PKP$) and waveform-based ($PKP$) data. Approximating the sensitivity by infinitely narrow rays is thus not appropriate, and, instead, we used 3-D sensitivity kernels, inferred from mode summation [*Zhao and Jordan*, 1998; *Zhao et al.*, 2000]. We did not use $P_{\mathrm{diff}}$ data from the *Engdahl et al.* [1998] catalog. We evaluated $PcP - P$ differential travel times, but because the data are noisy and not readily consistent with our mantle models, we decided not to use them for the construction of the models presented here.

We discuss the construction and use of 3-D sensitivity kernels and the selection, reduction, and combination of the waveform-based and routinely processed differential travel time residuals. We discuss the resolution of structure in the

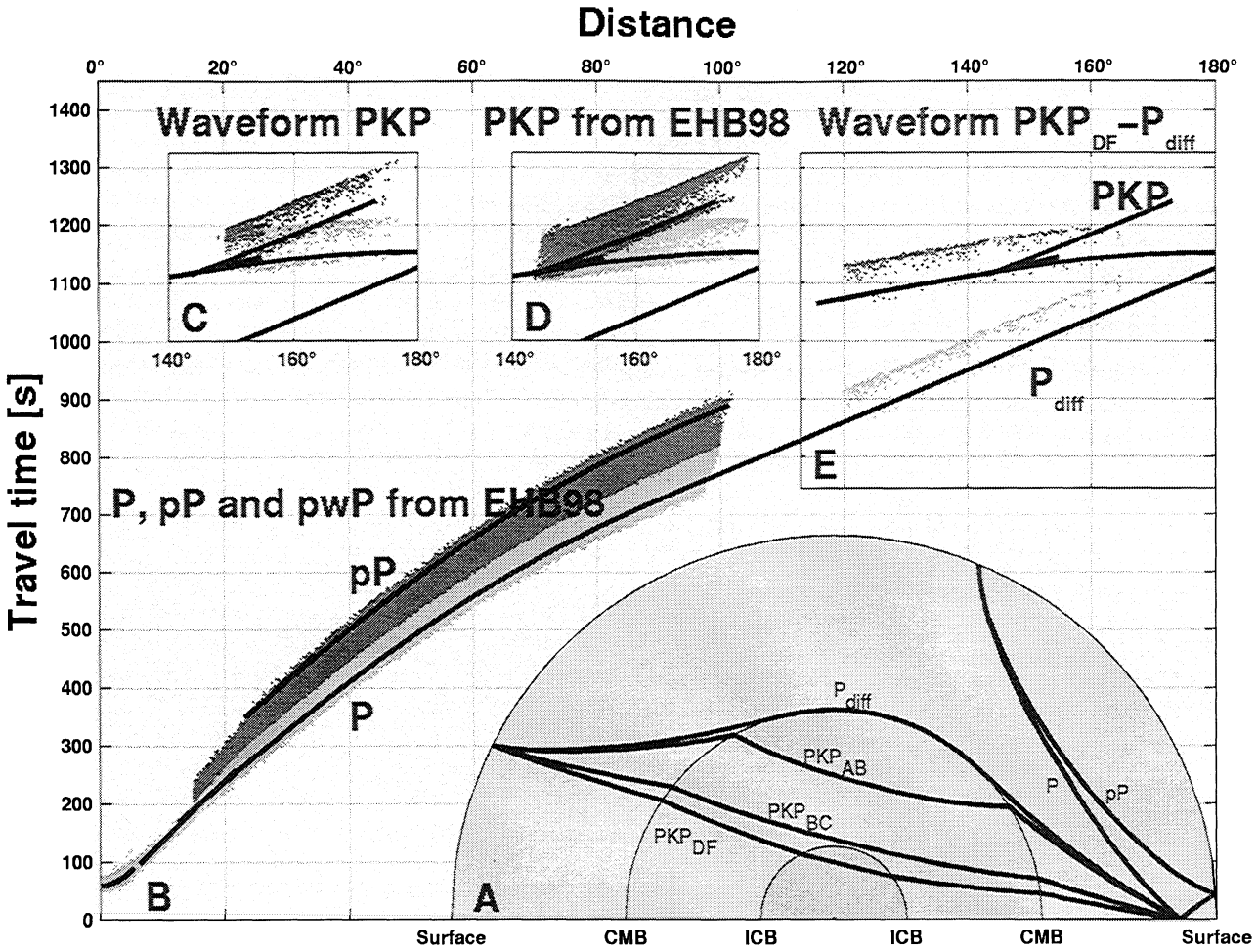


**Figure 1.** (a) The ray paths of the phases used in this study. $P$ is a direct $P$ wave that does not travel through the core, and $pP$ is reflected once off the surface. $PKP_{\mathrm{AB}}$ and $PKP_{\mathrm{BC}}$ travel through the outer core and $PKP_{\mathrm{DF}}$ travels both through the outer and the inner core. For $P_{\mathrm{diff}}$, the diffracted wave along the core-mantle boundary, we account for finite frequency effects by using 3-D kernels. (b) Travel times versus distance, (solid lines) theoretical curves for a earthquake at 500 km depth with respect to the ak135 model. Also shown are scatter plots for $P$ (light shading, ~7,000,000) and $pP$ (dark shading, ~430.000) from EHB98. (c) Same as Figure 1b except waveform based $PKP_{\mathrm{AB}}$-$P_{\mathrm{DF/BC}}$ (dark and light shading, respectively, 1383). (d) Same as Figure 1b except $PKP_{\mathrm{AB}}$-$P_{\mathrm{DF/BC}}$ from EHB98 (dark and light shading, respectively, ~ 27.000). (e) Same as (b) except waveform based $PKP_{\mathrm{DF}}$-$P_{\mathrm{diff}}$ (dark and light gray, respectively, 543). For detailed discussion of data sets, see text.

deep mantle and the potential trade off between mantle and core structure.

## 2. Data

### 2.1. $P$, $pP$, and $pwP$

Most of our data are selected from the routinely processed data set by *Engdahl et al.* [1998]. These, in turn, are based on bulletin data from the ISC and the U.S. Geological Survey's National Earthquake Information Center (NEIC). However, in an iterative nonlinear procedure, earthquakes were relocated, and for more than 60 different body wave phases the picks were reidentified using travel times according to the ak135 [*Kennett et al.*, 1995] reference model for $P$ wave speed. The data set is updated almost every year and the catalog used here comprises a total of nearly 14,000,000 phase arrival times from ~100,000 earthquakes that occurred between January 1, 1964, and December 31, 1998. The data reported to ISC and NEIC are measured from short-period (~1 Hz) records. Hereinafter this data set will be referred to as EHB98.

From the EHB98 data we used almost 7,000,000 $P$ and 430,000 $pP$ and $pwP$ travel time residuals (see Figure 1a for ray paths and Figure 1b for distance ranges), many of which have also been used in previous studies [e.g. *van der Hilst et al.* 1997; *Widiyantoro*, 1997; *Bijwaard et al.*, 1998]. We remark that the EHB98 data file contains more entries for these phases, but we have rejected those that were labeled as inaccurate by *Engdahl et al* [1998]. Hereinafter we refer to the EHB98 $P$, $pP$, and $pwP$, simply as EHB98 $P+$ data.

An advantage of the EHB98 $P+$ data is that data redundancy facilitates the extraction of structural signal, but a disadvantage of this and (most) other body wave data sets is the uneven sampling of the mantle. Upper mantle structure is well sampled near belts of high seismic activity and beneath dense receiver arrays, but large mantle volumes are poorly sampled, for instance in the upper mantle beneath intraplate regions and above the core mantle boundary beneath the Southern Hemisphere (Figure 2a).

### 2.2. Core Phases ($PKP$ and $P_{\mathrm{diff}}$)

To improve our ability to map the lowest few hundred km of the mantle we consider core refracted ($PKP$) and diffracted ($P_{\mathrm{diff}}$) waves (Figure 1). $PKP_{\mathrm{AB}}$ and $PKP_{\mathrm{BC}}$ travel through the outer core and $PKP_{\mathrm{DF}}$ goes both through the outer and the inner core. For $P_{\mathrm{diff}}$ the incidence angle is critical at the CMB so that the waves are diffracted along the core mantle boundary. $PKP$ data were used for tomographic imaging by *Vasco and Johnson* [1998]. $P_{\mathrm{diff}}$ data have been used to constrain lateral variations of $P$ wave speed [*Wysession*, 1996] but not in published 3-D studies.

**2.2.1. Differential travel time residuals.** For the core phases we consider differences in arrival time of two phases in a single seismogram. A differential travel time residual is the observed (obs) minus predicted (ak135) difference in travel time ($T$) of two phases in a single seismogram, which can be obtained from reported travel time residuals of the individual phases. For example, a $PKP_{\mathrm{AB}}$-$PKP_{\mathrm{DF}}$ differential travel time residual

$$\begin{aligned}\delta t_{PKP_{\mathrm{AB}}-PKP_{\mathrm{DF}}} &= (T_{PKP_{\mathrm{AB}}} - T_{PKP_{\mathrm{DF}}})_{\mathrm{obs}} - (T_{PKP_{\mathrm{AB}}} - T_{PKP_{\mathrm{DF}}})_{\mathrm{ak135}} \\ &= \delta t_{PKP_{\mathrm{AB}}} - \delta t_{PKP_{\mathrm{DF}}}. \end{aligned} \quad (1)$$

Differential times can also be measured by waveform cross correlation. In a single seismogram the waveform of one arrival can be used to predict that of another by accounting for attenuation and phase shifts. For example, the Hilbert transform of $PKP_{\mathrm{BC}}$ resembles the $PKP_{\mathrm{AB}}$ arrival since the latter passes through an internal caustic [*Jeffreys and Lapwood*, 1957; *McSweeney*, 1995]. Alternatively, the observed record can be cross-correlated with synthetic seismograms calculated by mode summation [*Woodward and Masters*, 1991; *Wysession et al.*, 1995] or ray theory [e.g., *Grand*, 1994]. In contrast to most travel time picks, such waveform cross correlations do not necessarily measure the first onset, but for measuring time differences this is not as serious a problem as for measuring absolute times.

Differential times can not be formed at all distances from the source, as can be seen from the travel time curves in Figures 1c-1e. This limits the number of data that can be used for imaging. However, in the distance range beyond which differential times can be formed all $PKP$ waves are of type $DF$, that is, they propagate through the inner core, and they have shorter ray segments in the deep mantle than any of the other $PKP$ phases, which makes them less attractive for the imaging of mantle structure. The use of differential travel time residuals has several important advantages. First, they are relatively insensitive to uncertainties in earthquake location and origin time and to heterogeneity in the shallow mantle, so that the contribution of the structural signal from the deep mantle can be isolated. However, the success of this isolation depends on ray geometry (and thus epicentral distance), on the (frequency dependent) width of the sensitivity zone around the ray, and on the length scale of aspherical earth structure. For instance, at midmantle depths the paths of $PKP$ and $P_{\mathrm{diff}}$ can differ by hundreds of kilometers (Figure 1a), which is more than the width of a Fresnel zone for a 1-Hz wave at that depth. Small scale structure in the mid mantle can thus be sampled preferentially along one of the paths, which can lead to bias if the differential times are interpreted as due to deep mantle structure only. Second, it serves as a data quality criterion. Multiple phase identification is less prone to phase misidentification, is only possible from records with high signal-to-noise ratio, and is probably only done by experienced seismic analysts.

**2.2.2. $PKP$.** For $PKP$ we use residuals determined both from the EHB98 catalog and from short-period digital seismograms using waveform cross correlation. *McSweeney* [1995] made 1383 short-period measurements and the EHB98 catalog yielded ~15,000 of $PKP_{\mathrm{AB}}$-$PKP_{\mathrm{BC}}$ and $PKP_{\mathrm{AB}}$-$PKP_{\mathrm{DF}}$ differential residuals.

From the EHB98 $PKP$ data we also from differential times The restriction to specific epicentral distances (Figure 1d) necessarily reduces the number of data that can be used; in our case from a total of $\sim 1.5\times 10^6$ to the ~54,000 that are used to construct ~27,000 differential times. Assuming that they are of higher quality than the routinely processed EHB data, we used the measurements by *McSweeney* [1995] to reduce the EHB98 differential travel time residuals. For a direct comparison of the two data sets we searched the EHB98 catalog for stations and events that were located in caps with a radius of 0.5° around the earthquake and station location in the waveform data set. Subsequently, we binned the qualifying EHB98 $PKP$ data and calculated the median of the residuals. Figure 3 shows the correlation (as a function of the number of EHB98 data within each bin) between the waveform based data and the medians of the EHB98 residuals thus selected. Good correlation is achieved for bins containing more than three paths. We processed all EHB98 $PKP$ data in a similar way: for every event-station pair we searched for other earthquake-station pairs within 0.5° caps and determined the median value of the selected residuals. Effectively, this creates a spatial moving average filter of the $PKP$ data. The use of bins with three or more hits significantly reduced the scatter (standard deviation decreased from 2.7 to 1.4 s) in the EHB98 $PKP$ differential times, but it further reduced the number of bundles of differential pairs used in the inversion to ~15,000.

For the data set used in our inversions we show in Figures 2c-2f the core entry and exit points for the two $PKP$ data sets. The potential for improving models of lower mantle $P$ wave speed with $PKP$ data is greatest in the Southern Hemisphere, e.g. beneath South America and the southwest Pacific, but many regions in the Northern Hemisphere benefit also, in particular beneath northern America, western Europe, and the Atlantic.

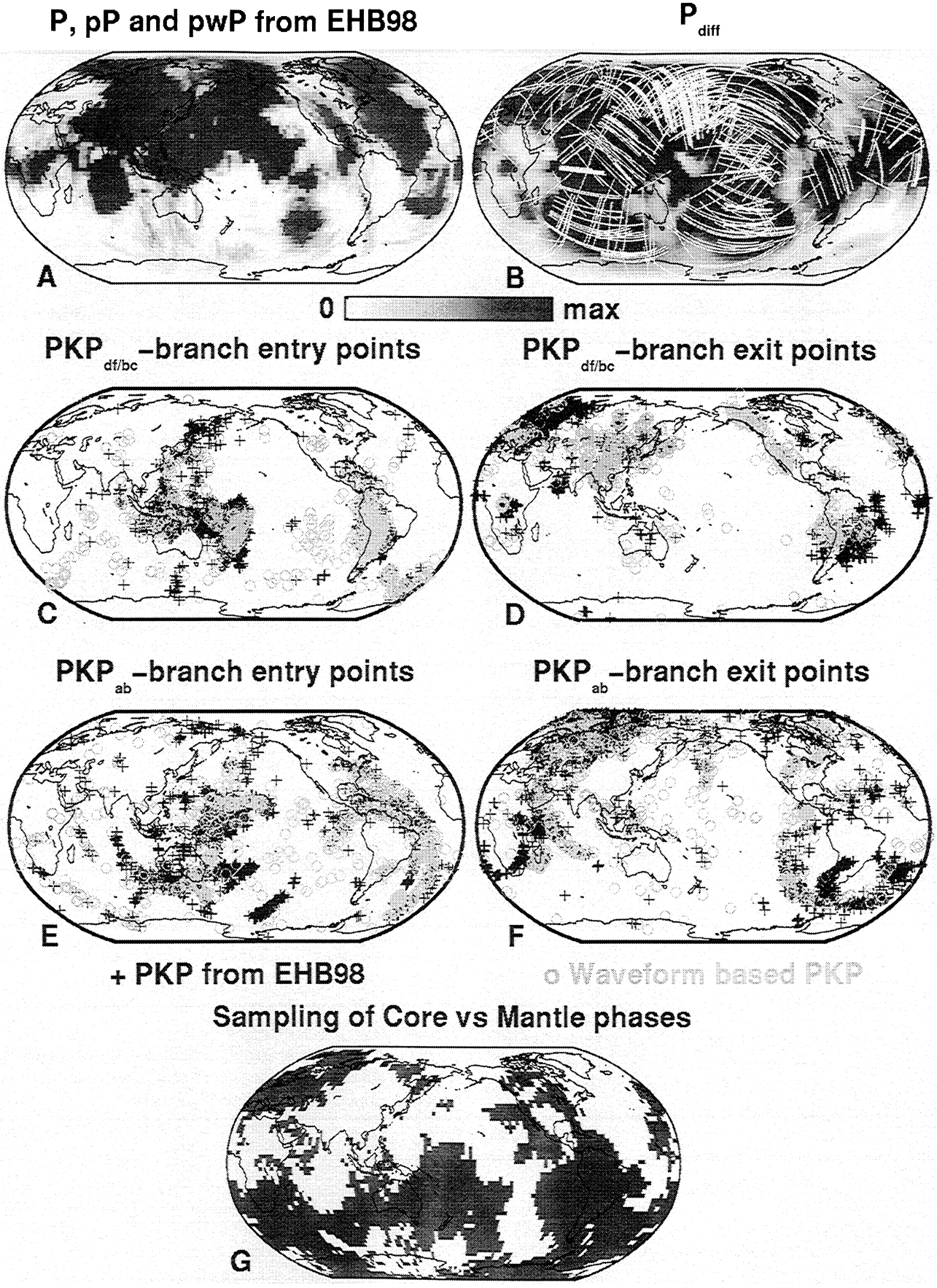


**Figure 2.** (a) The sampling of structure just above the CMB in terms of the (normalized) sum of ray segment lengths within each cell for EHB $P$, $pP$, and $pwP$. (b) Same as Figure 2a except $P_{\text{diff}}$ data. Note that for the construction of this figure we used the 3-D sensitivity kernels (see section 3.5). Also shown is the part of the optical ray that grazes the CMB (see Figure 1a). (c)-(f) Points of entry to and exit from the core for different branches of $PKP$ for both $PKP$ data sets. (g) Binary plot, showing as solid where the sum of the ray segments from all core phases exceeds the sum of EHB98 $P+$ ray segments.

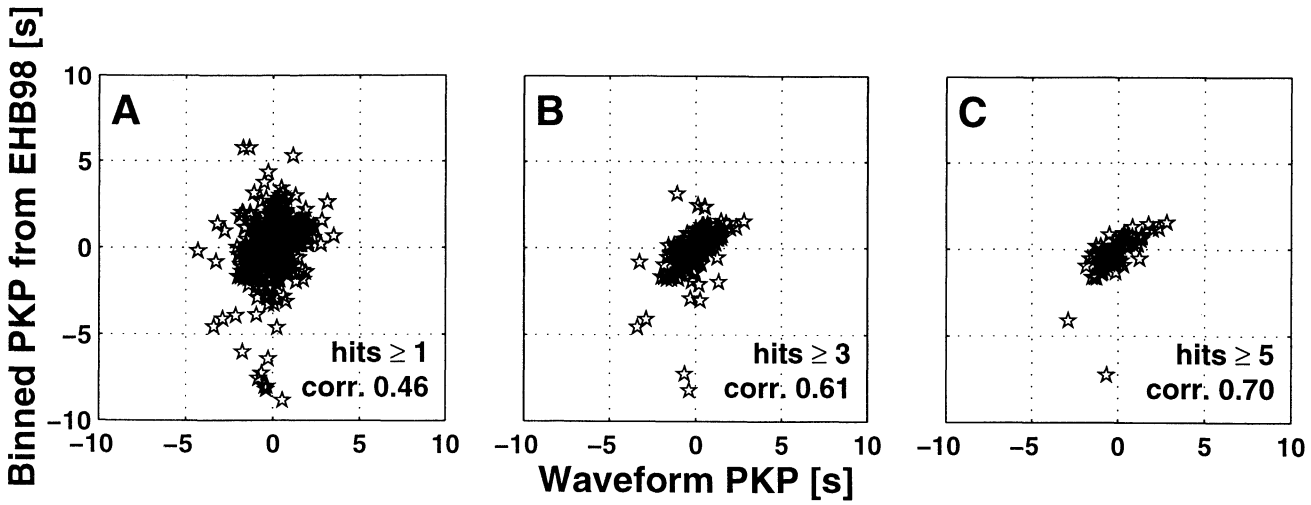


**Figure 3.** Correlation between raw residuals from waveform based $PKP$ data and the (medians of) binned $PKP$ residuals from EHB98. All medians (a) and medians with minimum three (b) and five (c) hits per bin.

**2.2.3. $P_{\text{diff}}$.** for the diffracted waves we do not use the EHB98 catalog. Instead, we use 543 $PKP_{\text{DF}}$-$P_{\text{diff}}$ measurements obtained by *Wysession* [1996] from long-period (~50 mHz) digital seismograms by waveform cross correlation. For these data, the epicentral distance range considered is 110° to 165° (Figure 1e). Diffraction cannot be described by ray theory, and a significant fraction of the work for this study was devoted to the design and implementation of 3-D sensitivity kernels (see section 3.5).

Figure 2b illustrates the effective data coverage in the deep mantle for long period $P_{\text{diff}}$. We also show the part of the corresponding optical $P_{\text{diff}}$ ray that grazes the CMB. Although the number of $PKP$ and $P_{\text{diff}}$ data is small compared to the number of EHB98 $P+$ data they are given a larger weight in the inversions (see below) and in many regions of the deep mantle they provide the only direct constraints.

**2.2.4. Effects of core structure.** $PKP$ residuals are sensitive to wave speed variations in the outer core, if any, and, for the $DF$ branch, to inner core structure [e.g., *Creager*, 1992; *Song and Helmberger*, 1995]. We omit $PKP_{\text{BC}}-PKP_{\text{DF}}$ differential times because they have small sensitivity to mantle structure. We further reduced the sensitivity of our data to inner core structure by correcting all $PKP_{\text{DF}}$ travel times for the inner core model by *Su and Dziewonski* [1995], although test inversions suggest that with the differential pairs used here the contamination of mantle structure by inner core signal would be small (see section 5.1).

The conventional view is that there is no significant heterogeneity in the outer core [e.g. *Jellinek et. al*, 1999]. *Kohler and Tanimoto* [1992] investigated velocity variations within the outermost 200 km of the core using $SKS$ and $SKKS$ waveforms and concluded that effects from mantle structure are hard to separate from core signal. *Vasco and Johnson* [1998] discussed the possibility of aspherical structure in the Earth's liquid outer core. Since such structure would effect the $PKP$ data used in our study, we investigated the trade-off between mantle and core structure with a series of inversion tests (see section 5.2). We conclude that explaining the core data do not require outer core heterogeneities. Therefore, except in specific tests we do not include the outer core in the inversions discussed here.

## 3. Methodology

### 3.1. Tomographic Problem

The purpose of travel time tomography is to interpret differences between observed and predicted (theoretical) travel times (that is, the "residuals") in terms of aspherical variations in wave speed (that is, "structure" or the "model") in Earth's interior. The inversion technique that we use, including the parameterization and the use of composite rays, is now fairly standard and is described in detail by, for instance, *Nolet* [1987] and *Spakman and Nolet* [1988]. Here we merely mention some basic aspects and discuss the integration of different data sets and the implementation of approximated 3-D sensitivity kernels.

Without the terms for regularization, the system of normal equations that describe the (linearized) relationship between model parameters and the data is given by

$$\mathbf{L}\Delta\mathbf{s} = \Delta\mathbf{t}. \tag{2}$$

The sensitivity matrix that contains the Fréchet derivatives, $\mathbf{L}$, contains the length of the ray segments in different cells and the partial derivatives for the simultaneous source location, $\Delta\mathbf{s}$ (the model vector) represents the slowness perturbation in the model space relative to an assumed reference model (ak135) and the change in hypocenter (origin time, longitude, latitude, depth), and $\Delta\mathbf{t}$ (the data vector) contains the travel time residuals. Using the iterative LSQR algorithm [*Paige and Saunders*, 1982; *Nolet*, 1985; *van der Sluis and*

*van der Vorst*, 1987], we invert $\mathbf{\Delta t}$ simultaneously for structure and for effects on source mislocation by minimizing the variance of the solution, $\sigma^2 = \epsilon^T \epsilon$, where $\epsilon = \mathbf{\Delta t} - \mathbf{L\Delta s}$ is the misfit between data and model predictions. The results shown here were obtained after 200 iterations, but with LSQR most of the convergence is achieved within a small number of iterations: ~98% of the final variance reduction was obtained after only 25 iterations.

There are many more data than model parameters, but the problem is underdetermined since a large part of the model space cannot be constrained because of uneven sampling. Moreover, the system of equations is inconsistent owing to data noise. Consequently, there is no unique solution and we need to use regularization (damping). We apply norm damping, which suppresses anomalies in poorly constrained cells and thus biases to a lower amplitude solution, and gradient (first derivative) minimization, which enforces smooth variations in latitudinal and longitudinal directions. No regularization is used in radial direction.

### 3.2. Parameterization

The model ($\mathbf{\Delta s}$) is usually described by a linear combination of orthogonal basis functions that span the model space of interest. Many global studies have used global basis functions, such as spherical harmonics [e.g. *Su et al.*, 1994; *Li and Romanowicz*, 1996; *Masters et al.*, 1996]. Here, we follow *Inoue et al.* [1990], *Pulliam et al.* [1993], *Vasco et al.* [1994, 1995a], *Grand et al.* [1997], *van der Hilst et al.* [1997], *Vasco and Johnson* [1998], *Bijwaard et al.* [1998] and many others and use a cellular representation with nonoverlapping constant wave speed blocks in longitude, latitude, and radius. Both representations have specific advantages and disadvantages. A local basis facilitates the suppression of artifacts in regions of no data coverage [*Boschi and Dziewonski*, 1999] and allows efficient regionalization [*Abers and Roecker*, 1991; *Bijwaard et al.*, 1998; *Kárason and van der Hilst*, 2000]. However, the number of parameters often is too large for exact inversions so that such approaches have to resort to iterative methods, which involve somewhat subjective criteria for convergence and regularization and do not allow the calculation of a resolution matrix.

Since the objective here is to improve the constraints on deep mantle structure by inclusion of core phases, no attempt was made to optimize the solution for small scale structure, such as slabs, in the upper mantle. For the parameterization of the mantle we use a regular 3-D grid consisting of 20 layers, each ~150 km thick, which are divided into 7200 3°×3° latitude and longitude cells. For the assessment of

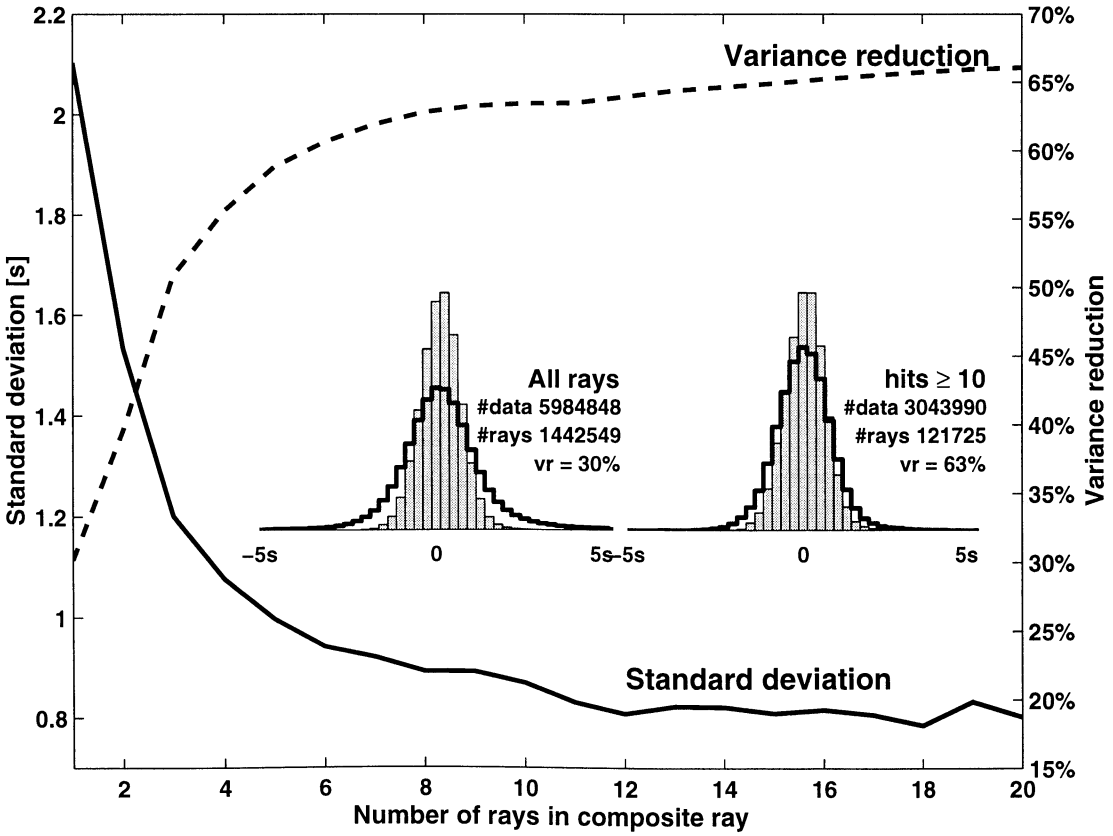


**Figure 4.** Standard deviation (solid line) of the median of travel time residuals from individual rays in a composite ray as function of number of rays in a composite ray. Variance reduction (vr) (dashed line) as function of minimum number of rays per composite ray used in the calculation. Histograms (inset plots) showing the distribution of original residuals (solid line) and model produced residuals (shaded bars) for all composite rays and for composite rays with 10 or more hits.

the trade-off between mantle and core structure (see section 5) we performed test inversions with a $10°\times10°$ lateral grid in 6 (2) layers in the outer (inner) core.

### 3.3. Composite Rays and Variance Reduction of EHB98 $P+$ data

To suppress random noise in ISC picks we use the redundancy in the almost $7\times10^6$ EHB98 $P+$ residuals and construct "composite rays" [*Spakman and Nolet*, 1988]. We trace the ray for each earthquake that is located in a mantle volume of $1°\times1°\times75$ km to a station located in a receiver cluster, but the path is always added to the same row of the sensitivity matrix $\mathbf{L}$. Such ray bundles, or "composite rays", better represent the sampling than single "summary rays" that connect an earthquake and station cluster. However, a comparison between the results based on either approach reveals little difference [*Widiyantoro*, 1997]. For the inversions we used almost $1.5\times10^6$ $P$ and almost 220,000 $pP$ and $pwP$ composite rays. For the processing of the EHB98 differential $PKP$ times see section 2.2.2.

We do not restrict the number of individual rays that form a composite ray. Some bundles comprise more than 1000, but the average is about four. To suppress effects of outliers we use the median of the residuals as the datum associated with such a ray bundle. In order not to bias the distribution, we do not discard data prior to calculating the medians; however, composite rays with medians that have absolute values in excess of 5 s are excluded to reduce further the effects of outliers (this concerns $<1\%$ of the original data set). Increasing the number of rays that constitute a composite ray results in a decrease of the spread of the associated residuals (Figure 4, solid line). We scale each matrix row so its total path length equals the square root of the sum of path lengths for all rays that constitute the composite ray and weight the residual accordingly. This is roughly equivalent to using the individual rays but repeating the median residual in a least squares inversion. However, beyond the first 10 or so rays the net gain of adding more measurements diminishes because effects of, for instance, earthquake mislocation, instrumentation, near receiver structure, and imperfect theoretical approximations begin to overshadow the random reading errors. Therefore we apply a constant weight ($\sqrt{10}$) to all composites with 10 or more rays. Although only 10% of the composite rays get the highest weighting they comprise more than 50% of the data.

Figure 4 shows that the variance reduction upon tomographic inversion, defined as $\mathbf{1}-\mathrm{Var}\,(\boldsymbol{\epsilon})/\mathrm{Var}\,(\mathbf{\Delta t})$, (dashed line) is small for composite rays with very few entries. If all composite rays are included, irrespective of the number of rays within them, the variance reduction for the (composite ray) residuals is $\sim$30%. However, our weighting increases the influence of ray bundles with a larger number of rays, and for the composite rays with more than 10 hits (which involves about 50% of the data) the variance reduction is 63% and the frequency distributions of $\mathbf{L\Delta s}$ versus $\mathbf{\Delta t}$ are similar (see Figure 4, inset). The variance reduction of the $7\times10^6$ or so individual data is thus somewhere between 30% and 63%.

### 3.4. Weighting of Waveform Data

The regularization of the inversion problem depends largely on the sampling and the noise level of the largest data set, and small data sets, even high-quality ones, can only exert influence if given more weight than individual entries in the routinely processed EHB98 catalog. Each $PKP$ and $P_{\mathrm{diff}}$ waveform measurement gets a weight equal to a composite ray containing 10 or more rays (i.e., $\sqrt{10}$).

### 3.5. Fresnel Zones and Sensitivity Kernels

The volume about the geometrical ray path between source and receiver that contributes significantly to the recorded seismogram is related to the Fresnel zone. In homogeneous media the maximum width ($w_m$) of the Fresnel zone can be approximated by ray geometry [*Nolet*, 1987]:

$$w_m = \sqrt{\frac{\lambda S}{2}}, \tag{3}$$

where $\lambda$ is the wavelength and $S$ is the total path length from source to receiver. In general the width of the Fresnel zone thus increases with decreasing frequency (increasing $\lambda$) and with increasing distance between source and receiver. With few exceptions [e.g., *Vasco et al.*, 1995b] such Fresnel zones are not used in travel time tomography. Instead, one usually calculates the Fréchet derivatives (i.e., the elements of matrix $\mathbf{L}$) by simple ray tracing and applies damping or imposes some spatial correlation length to obtain a smooth result. This avoids a major computational effort, it is adequate when high frequency waves are used since then the Fresnel zones are relatively small. For a frequency of $\sim$1 Hz the width of a Fresnel zone for a $P$ wave that bottoms just above the CMB is $\sim$200 km, which is slightly larger than the cell size used in our inversions but less than the length scale of structure we expect to resolve. Moreover, the use of composite ray bundles also results in the distribution of the sensitivity over neighboring cells and further smoothing can be accomplished by regularization.

For the interpretation of the $PKP_{\mathrm{DF}}$-$P_{\mathrm{diff}}$ residuals the ray theoretical approximation is not satisfactory. They are deduced from records with a central frequency of $\sim$50 mHz, which implies a $\sim$1000 km Fresnel zones for waves that just touch the CMB and much more for the diffractions around the core. Furthermore, $P_{\mathrm{diff}}$ is not a ray geometrical phase: it is an evanescent and dispersive wave at the CMB so that the travel time and its sensitivity to structure are frequency-dependent.

*Zhao and Jordan* [1998] and *Zhao et al.* [2000] calculated frequency-dependent sensitivity kernels with a stationary phase approximation and normal mode summation with cross-branch mode coupling. An example of a $P_{\mathrm{diff}}$ kernel is shown in Plate 1a. The sensitivity is concentrated near the ray theoretical path. However, the cancellation of energy away from the ray (resulting from destructive interference of the modes) is not perfect, which is mostly due to the fact that the limited number of the modes and the finite frequency bandwidth used in the summation prevents the complete isolation of the low amplitude $P_{\mathrm{diff}}$ phase from other,

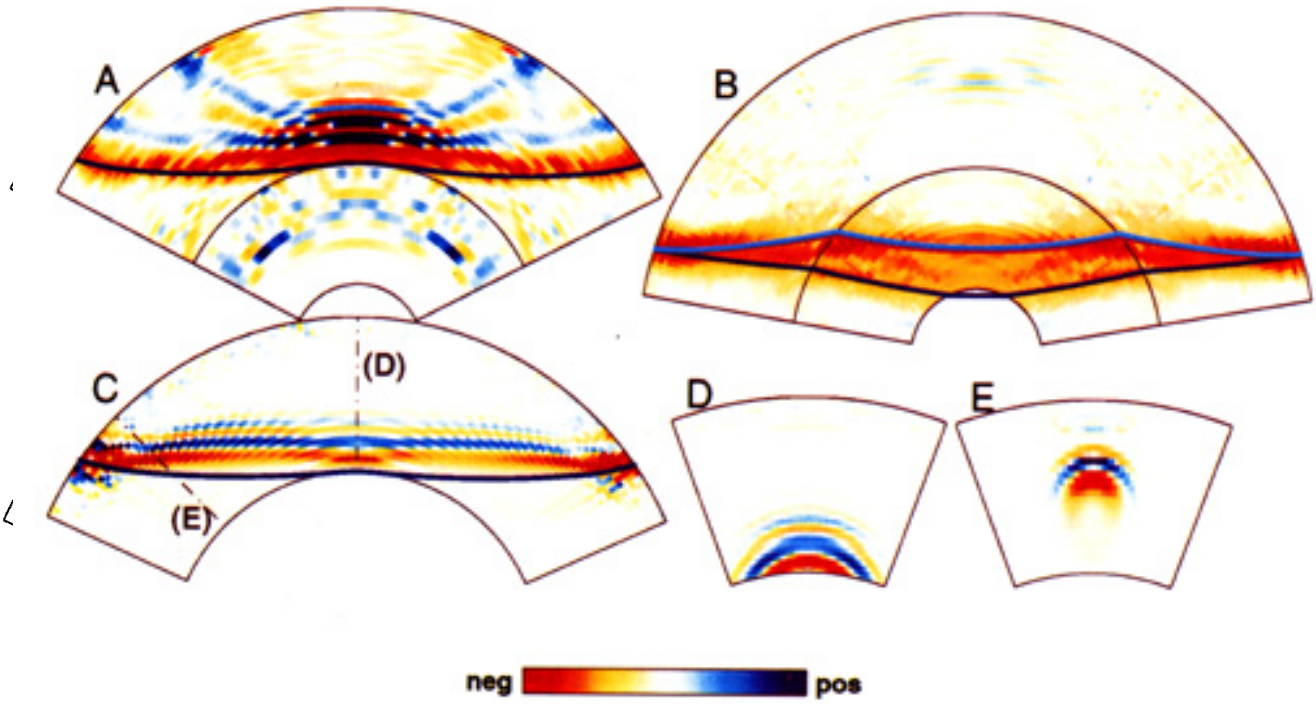


**Plate 1.** (a) Fréchet kernel in the event-station great circle plane showing sensitivity to wave speed variations within the earth for $P_{\text{diff}}$ phase. Alternating red and blue indicate the first, second, etc, fresnel zone. (b) Same as Plate 1a except for $PKP$. (c) Same as Plate 1a except $S_{\text{diff}}$ through a smoothed earth model. (d) and (e) Fréchet kernels along lines shown in Plate 1c.

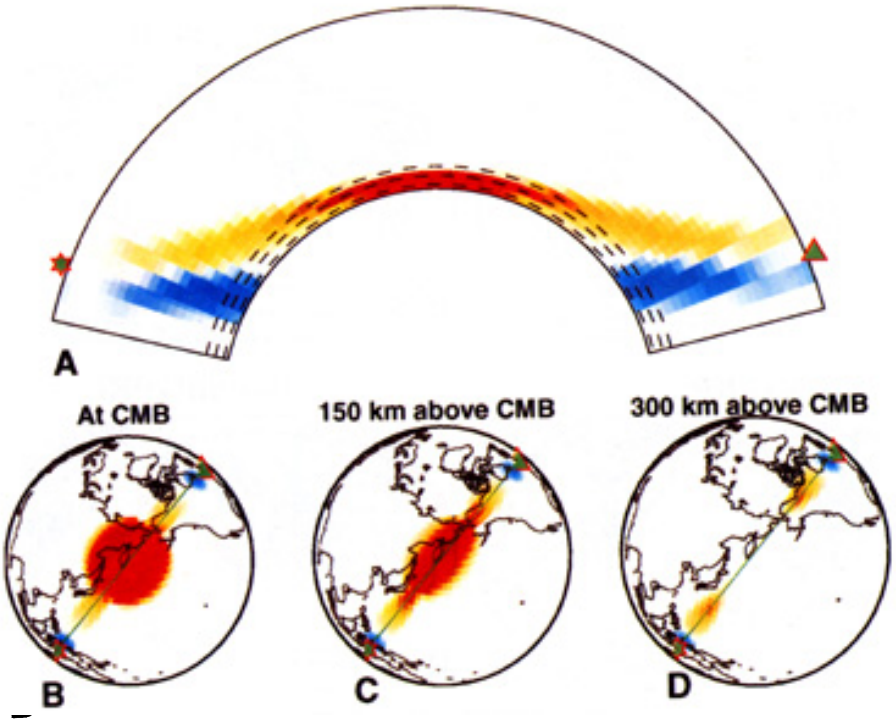


**Plate 2.** Sensitivity to slowness variations within the Earth using differential times. Red and blue indicate negative and positive sensitivity as one kernel is subtracted from the other to give sensitivity to differential times. (a) Cross section along the great circle connecting event (star) and station (triangle) from $P_{\text{diff}}$ data file. (b)-(d) Three deepest layers of sensitivity kernel in map view.

often more energetic arrivals, such as $PP$. Plate 1b shows the sensitivity kernel for the travel time of $PKP$. For this epicentral distance the difference in arrival time for the three branches of $PKP$ is small and at a frequency of 50 mHz it is not possible to isolate them from each other. The sensitivity away from the ray is suppressed more effectively than in the case of $P_{\mathrm{diff}}$ because $PKP$ is a distinct high energy arrival.

To illustrate further the complex morphology of sensitivity kernels of core diffracted waves, we show in Plate 1c a great circle section through a 3-D kernel of $S_{\mathrm{diff}}$, calculated for the transverse (*SH*) component, and in Plates 1d and 1e we depict the kernel in sections perpendicular to the ray path (at locations d and e in Plate 1c). For this calculation, *Zhao et al.* [2000] used an earth model based on 1066A [*Gilbert and Dziewonski*, 1975]. Interestingly, most of the sensitivity for diffracted phases is located above the ray; energy in waves heading deeper than the critical ray is refracted away from this ray path and does not contribute to the record as observed at the receiver. (Note that this should make the long-period diffracted waves virtually insensitive to topography of the core mantle boundary.) Plates 1d and 1e illustrate the broadening of the sensitivity kernel above the CMB; the maximum width of the kernel increases with increasing epicentral distance and is largest for $\Delta$=180° when it covers almost the entire surface of the core.

The calculation of 3-D Fréchet kernels for each data point is not practical for large data sets. For computational efficiency we developed analytical expressions that match the 'true' kernels (calculated for three epicentral distances only) and designed an algorithm to project them onto the basis functions that define the model space. Plate 2 illustrates such an approximated kernel. The sensitivity is distributed over many cells around the ray and is scaled so that the total travel time is correct for a given 1-D Earth model. Plate 2a shows that the sensitivities of $PKP_{\mathrm{DF}}$ and $P_{\mathrm{diff}}$ cancel in the shallow mantle and that the maximum sensitivity of the travel time residual is reached near the base of the mantle. Notice, however, that even for these long-period differential times the sensitivity to midmantle structure along both the $P_{\mathrm{diff}}$ and the $PKP$ path is not negligible. Plates 2b-2d show the change in sensitivity with increasing distance from the CMB.

Although our analytical functions are mere approximations, we prefer them over narrow ray paths because they allow us to deal with the frequency dependance of $P_{\mathrm{diff}}$ sensitivity kernels and to account for the differences in Fresnel zone width in the data space instead of accomplishing the required smoothing in the model space which would also prevent the short-period data from constraining small-wavelength structure.

## 4. Results

### 4.1. Models From Different Data Sets

We use the layer just above the CMB to illustrate the influence of the individual data sets on the images (Plate 3).

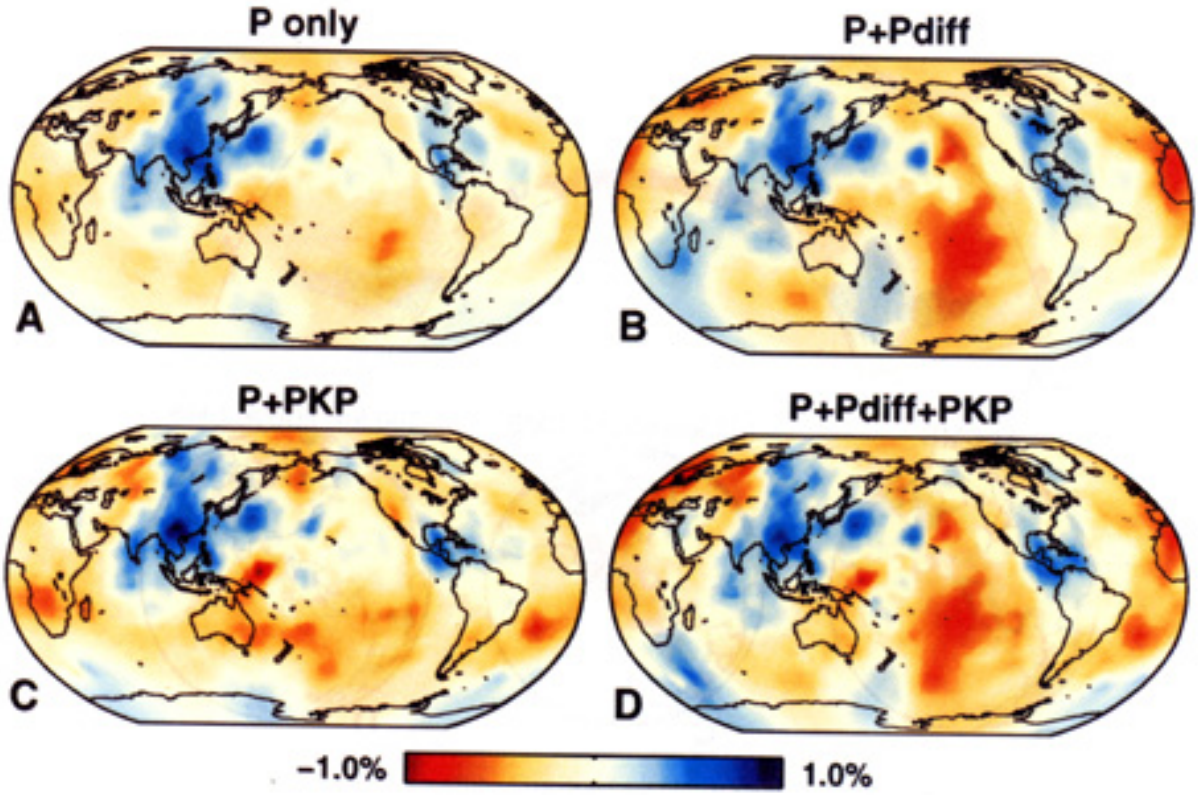


**Plate 3.** Deepest layer, centered around 2819 km depth for models based on different combinations of data sets. (a) KH2000PM: Model based on EHB $P+$. (b) P+$P_{\mathrm{diff}}$: EHB $P+$ and $P_{\mathrm{diff}}$ data. (c) P+PKP: EHB $P+$ and both waveform based $PKP$ and $PKP$ from EHB98 data. (d) KH2000PC: Model based on all data sets.

Plate 3a depicts the solution based on EHB98 $P+$ data only (KH2000PM). The inclusion of the $PKP_{DF}$-$P_{diff}$ significantly enhances the slow anomalies beneath the Pacific and west Africa and introduces high wave speed anomalies beneath southern Africa and the Tasman Sea (Plate 3b). We remark, however, that the deepest mantle beneath southern Africa is not well sampled by either of the data sets used (see also section 4.3). When the $PKP$ data are inverted along with EHB98 $P+$ data, the fast structures beneath the Caribbean and at high latitude in the Southern Hemisphere become stronger and so do the slow anomalies beneath Africa and the western Pacific toward Australia (Plate 3c). The solution based on all data (KH2000PC) (Plate 3d) is in good agreement with the result based on EHB98 $P+$ alone, but several anomalies are now more prominent, in particular, beneath the Southern Hemisphere, as expected from the complementary nature of data coverage (Figure 2), and the overall amplitude of the anomalies has increased.

### 4.2. Compatibility of the Different Data Sets

We assessed the success of the integration of the different data sets by quantifying how well a particular subset of data is explained by the 3-D mantle models constructed with or without the data under evaluation. In Figure 5 we compare for different data sets the observations ($\mathbf{\Delta t}$) and model predictions ($\mathbf{L\Delta s}$), with $\mathbf{L}$ the sensitivity matrix for the data set to be tested. In Figure 5 the left column shows the predictions by KH2000PM based on EHB98 $P+$ only but all data were used for KH2000PC that render the fits in the right column. We show only residuals for composite rays with 10 or more rays to allow a direct comparison with waveform data. The models fit the EHB98 $P+$ data well, even though there is still a significant fraction of the signal that is not explained [see also *Bijwaard et al.*, 1998].

Similar to our previous models [e.g., *van der Hilst et al.*, 1997], the model based only on EHB98 $P+$ significantly underestimates the structural signal in the core phases (Figure 5, left). From $PKP$ data fit, *Song and Helmberger* [1997] argued that the model by *van der Hilst et al.* [1997] underestimates the amplitude of deep mantle structure by up to an order of magnitude. *Van der Hilst et al.* [1998] confirmed this conclusion but also showed that the pattern of $PKP$ residuals measured by *McSweeney* [1995] is consistent with the model by *van der Hilst et al.* [1997], which argues against data errors as the prime explanation for the amplitude discrepancy. Our model probably underestimates the amplitude of the wave speed perturbations owing to parameterization by means of constant (i.e., average) wave speed blocks and to regularization, in particular in regions of poor data coverage. For the model, in general, the amplitude amplification implied by *Song and Helmberger* [1997] is not realistic, but a substantial increase is possible in areas sampled by the $PKP$ used in their analysis but not by our EHB98 $P+$ data. By including the core phases in our tomographic inversion we improve the fit (Figure 5, right), in particular of the waveform based $PKP$ differential travel time residuals (Figures 5b and 5c).

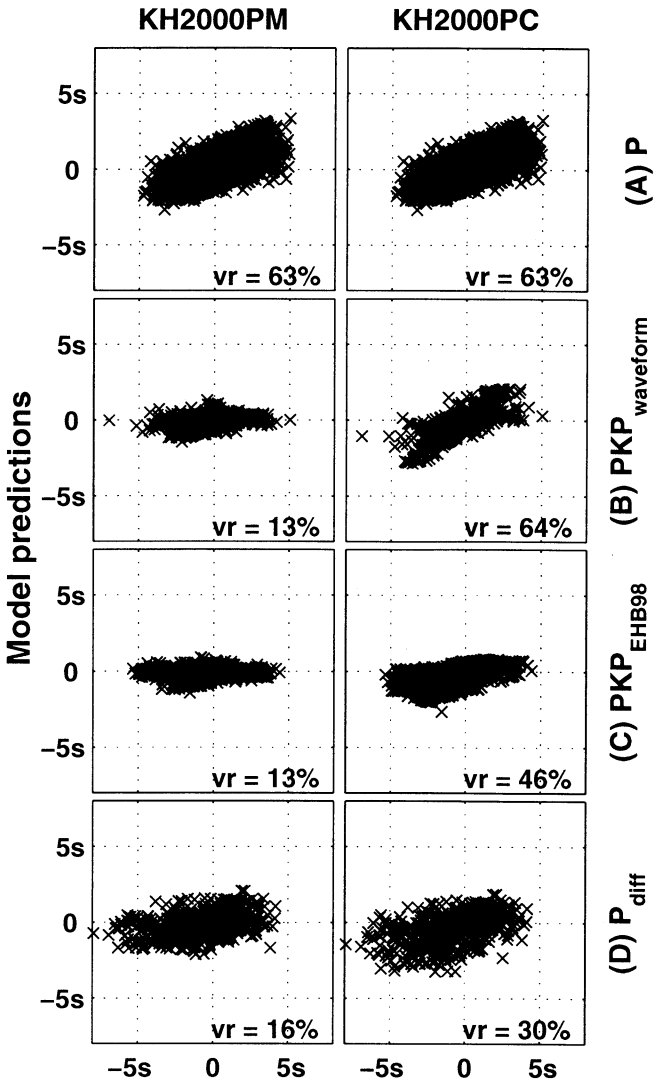


**Figure 5.** Scatterplots, original residuals vs model predicted residuals. (left) Model KH2000PM. (right) Model KH2000PC. (a) EHB98 $P+$ residuals from EHB. (b) residuals from waveform based $PKP$. (d) $PKP$ residuals from EHB98. (d) $P_{diff}$ residuals.

Figure 5 demonstrates that the joint inversion has significantly improved the fit of the core phases without degrading the fit of $P$ data itself. The smallest variance reduction is achieved for $P_{diff}$ (Figure 5d): 16% when they are not included and 30% when they are. Since the $P_{diff}$ signal is averaged over large Fresnel zones the small variance reduction suggests that we still underestimate the amplitude of long-wavelength structure in the lowest mantle. However, we decided not to weight this data set further because effects on the sensitivity kernels of CMB topography, earthquake mechanisms, and radiation patterns, and unmodeled finite-frequency effects may combine to a larger uncertainty.

### 4.3. Resolution

In addition to quantifying the data fit we have investigated how the addition of the extra data increases our ability to

reconstruct Earth's structure. Calculation of even an approximate resolution matrix is computationally very expensive [*Nolet et al.*, 1999; *Vasco et al.*, 1999]. With our inversion method we performed test inversions with synthetic data calculated from different input models by multiplying the sensitivity matrix with the input structure, $\mathbf{\Delta t_{syn}} = \mathbf{L\Delta s_{syn}}$. We used the same regularization as for the inversion of the observed data. We performed two sets of inversion tests. In both cases the input model is a layer consisting of sinusoidal wave speed variations with a peek wave speed perturbation of 2% (see scalebar and input patterns at the bottom of Plate 4). The first set has half wavelengths ranging from ~1800 km at the CMB up to ~2800 km at 1000 km depth. The second test has half the wavelength of the first one. Plates 4a-4d show, at the same scale as the input models, the recoveries of such a pattern placed at depths of 1000, 1500, 2000 km, and just above the CMB. For the CMB we show the result from the longer-wavelength test since structures with characteristic length ~900 km are on the margin of our resolving power.

These results were obtained using all data, that is the EHB98 $P+$ and the $PKP$ and $P_{\text{diff}}$ differential travel time residuals. With the caveat that such tests primarily depend on ray coverage and do not account properly for data error, these results suggest that the lateral resolution of structure at wavelengths is excellent beneath most geographic regions, except beneath the central Pacific and the higher latitudes of the Southern Hemisphere. We remark that lateral resolution does not seem to change much between 1000 and 2000 km depth, but it deteriorates toward the base of the mantle (beneath 2500 km depth).

Of our primary interest is to what extent the added data improve our ability to recover structure in the deep mantle. Plate 4e displays the result of a test inversion with EHB98 $P+$ data for a target just above the CMB using the longer wavelength pattern. Plate 4f shows the difference between this result and the recovery obtained when the core phases are included (Plate 4d). Visual inspection of Plates 4d and 4e shows that overall the recovery of both the heterogeneity pattern as well as the amplitude improves when the core phases are included. In many regions the improvement is small, but, as expected from the differential sampling (Figure 2g), the recovery is improved beneath South and Central America, Europe, north Asia, and the Australia-western Pacific region (Plate 4f). In these regions the structure, the lateral gradients, and the amplitudes are better reproduced. We remark, however, that even after addition of the new data the recovery remains problematic south of South Africa and in the southern Pacific.

To quantify the gain from the additional data, we calculated the change in model variance by subtracting the recovery from the input model; this measure is mostly sensitive to amplitude differences. Furthermore, we performed a point-by-point correlation between the input and output model, which provides a measure of the match in heterogeneity pattern. The laterally averaged values of the variance reduction and correlation are shown in Figure 6a as a function of depth for both tests. These results suggest that on average, and in most of the depth range of the lower mantle, we recover ~70% of the true variance and match ~90% of the long wavelength heterogeneity pattern (solid lines) if the core phases are included. Near the base of the model these values drop to ~55% and ~85% for amplitude and pattern, respectively, suggesting that we can map the geographic distribution of wave speed variations rather well, but even with the core phases added, we underestimate, on average, the true amplitude by as much as a factor of 2. The effect of adding the $PKP$ and $P_{\text{diff}}$ becomes noticable at ~2000 km depth, but it remains small until we reach the bottom 300 or so km of the mantle; without the core phases, only 45% of the variance is recovered and only 75% of the pattern. It is harder to resolve the smaller scale structure (Figure 6a shaded lines) and the gradient damping, which suppresses sudden changes, becomes more dominant as the wavelength decreases. Still the correlation remains fairly high (~70% for most of the lower mantle), indicating a reasonable pattern match, but the variance reduction decreases from ~40% → ~20% towards the CMB.

The input models have structures only in the specific layer that is being tested but during the inversion some signal is "smeared" to other layers. We investigated this radial smearing by calculating the root-mean-square (rms) of the recoveries, layer by layer, as can be seen in Figure 6b for the longer-wavelength test with all phases. All the values shown here, including the input (shaded bars), are relative to the recovered rms of the layer being tested. As is to be expected with steeply descending rays the ability to constrain the radial extent of structures is smallest in the top few hundred kilometers. The radial smearing is however similar over the most of the lower mantle and no significant deviations in the depth interval 1000 km to 2500 km are apparent; both the rms of the recovery in the input layer and the level that is smeared to adjacent layers are fairly constant. In the deepest of mantle the smearing is still similar, but the recovered rms is slightly lower, consistent with Figure 6a. The short wavelength test gives a similar result except for lower rms in the recovery.

These inversion tests should, however, be interpreted with caution [*van der Hilst et al.*, 1993]. First, such tests primarily reflect data coverage but do not assess the influence of data quality. Second, we do not know the true noise level of the data, which makes it hard to judge what level of damping is needed for such experiments and how (systematic) errors propagate into the model. Third, resolution assessed this way depends on the length scale of the input heterogeneity [*Lévêque et al.*, 1993]. Ideally one would calculate the resolution kernel for each model parameter but that is computationally prohibitive and even approximations take a long time to calculate [*Nolet et al.*, 1999; *Vasco et al.*, 1999]. Finally, implicit in the way the test inversions are conducted is that we know the propagation paths and the earthquake locations so that the nonlinearity of the problem is much less severe. In particular, we use the same (linear) theory for the

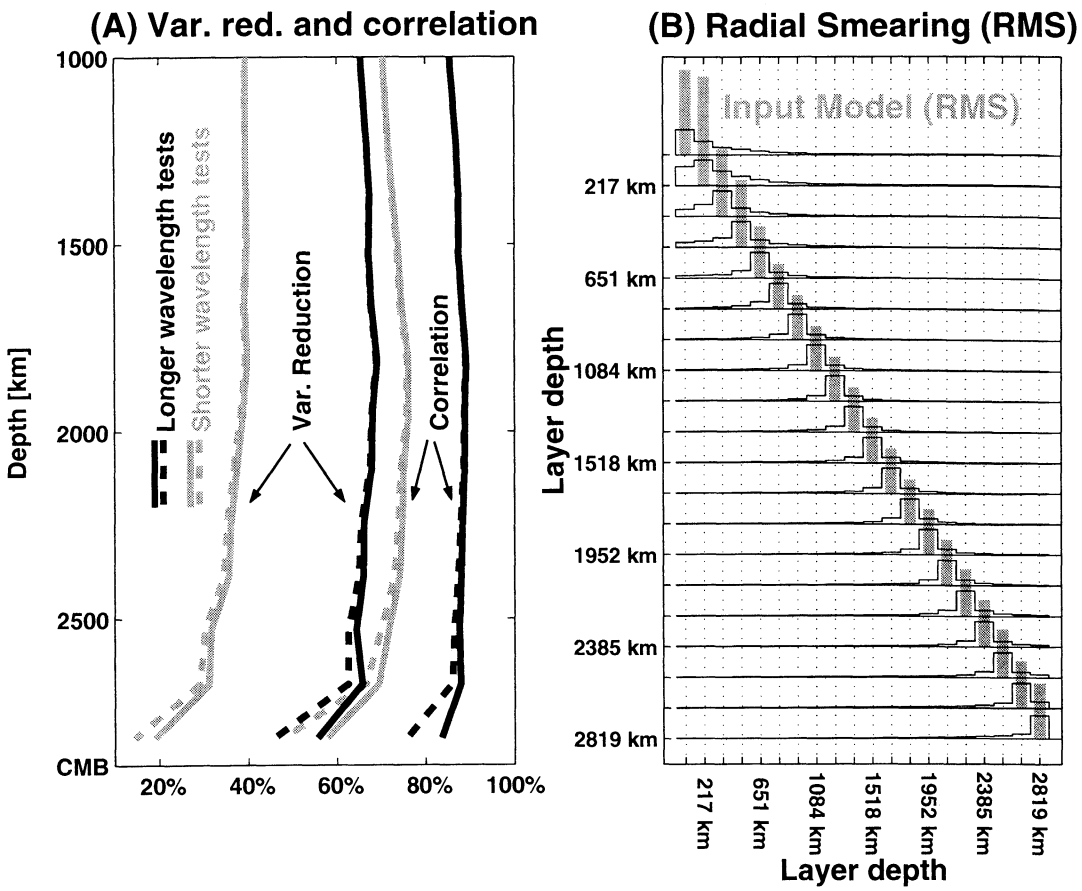


**Figure 6.** The two pairs of curves on the right depict correlation as function of depth. Solid unbroken line: Correlation between the longer wavelength input pattern (Plate 4, inset) and the recovery using mantle and core phases (e.g. Plate 4d). Solid dashed line: Same except using mantle phases only (e.g. Plate 4e). Shaded lines: Same as solid lines except for the shorter wavelength pattern (Plates 4a-4c and inset). The two pairs of curves on the left depict variance reduction. Solid unbroken line: The reduction of variance when subtracting the recovery from the input pattern using mantle and core phases. Solid dashed line: Same except using mantle phases only. Shaded lines: Same as solid lines except for the shorter wavelength pattern. (b) Vertical smearing as inferred from resolution tests with the longer wavelength structure (shaded bars) placed in one layer at a time. The recovery reveals some "smearing" to adjacent layers (solid lines). Values are scaled relative to the maximum rms of the recovery.

synthesis and the back-projection of the data, and for both the forward and inverse problem the Earth is assumed to be isotropic.

### 4.4. Lower Mantle $P$ Wave Speed

Selected layers from the final model are shown in Plate 5. The long and narrow features that emerge in the upper mantle transition zone are prominent around 1500 km depth beneath North and South America and beneath the southern margin of Asia. These have been associated with plate motion history and are thought to be the remnants of old subducted slabs [*Woodhouse and Dziwonski*, 1989; *Grand*, 1994; *van der Hilst et al.*, 1997; *Grand et al.*, 1997]. At larger depth these structures seem to disintegrate and at about 2000 km no such large coherent fast structures are visible. Our resolution tests (e.g., Figure 6b) indicate that these observations can not simply be explained by changes in data coverage or "smearing" in radial direction. Indeed, *Kárason and van der Hilst* [2000] show that beneath many of the major convergent plate boundaries slabs of subducted lithosphere lose their wave speed signature (or disappear althogether) near 1,800 km depth. Judging from Plates 4a-4d and Figure 6 those changes cannot easily be attributed to differences in data coverage. In accord with other models [e.g., *Liu and Dziewonski*, 1998; *Castle et al.*, 2000] we find that the pattern of heterogeneity near the base of the mantle persists to several hundreds of kilometers above the CMB; it does not connect to the midmantle pattern but gradually breaks down and is absent at depths $<\sim$2300 km. However, some slow anomalies probably extend to much larger distances above the CMB [e.g. *Ritsema et al.*, 1998, 1999; *Mégnin and Romanowicz*, 2000].

Near the base of the mantle the most prominent features are the fast anomalies beneath Central America and Asia and

the slow anomalies beneath the Pacific, west Africa, and the South Atlantic. This structure is generally consistent with results of shear wave tomography (although differences exist, notably beneath Australia and Alaska where shear wave speed is high and $P$ wave speed low) but has not been borne out so well by our previous $P$ inversions. In a spectral analysis the structures of higher-than-average $P$ wave speed around the Pacific would strongly contribute to a spherical harmonics degree 2 signal, but it is probably not a continuous structure.

Figure 7 shows the rms of the models without and with core phases (KH2000PM and KH2000PC, respectively) and the correlation between them as function of depth. Comparison of the images (Plate 5) and analysis of model correlation (Figure 7, shaded dashed line) and radial changes in rms amplitude (Figure 7, black lines) reveals that the models are nearly identical in structure and amplitude to a depth of about 1500 km. At larger depths the models slowly become more distinct and, in particular, the rms amplitude in model KH2000PC increases much more rapidly with depth than in model KH2000PM (Figure 7), especially in the slow regions. The correlation between the two models (Figure 7) begins to decrease at ~1500 km depth, whereas the lateral resolution is the same to ~2000 km depth (Figure 6a). This discrepancy is probably due to small scale (few hundred kilometers) structure that was not represented in the checkerboard models used and to smearing along the mantle legs of $PKP$ and $P_{\mathrm{diff}}$.

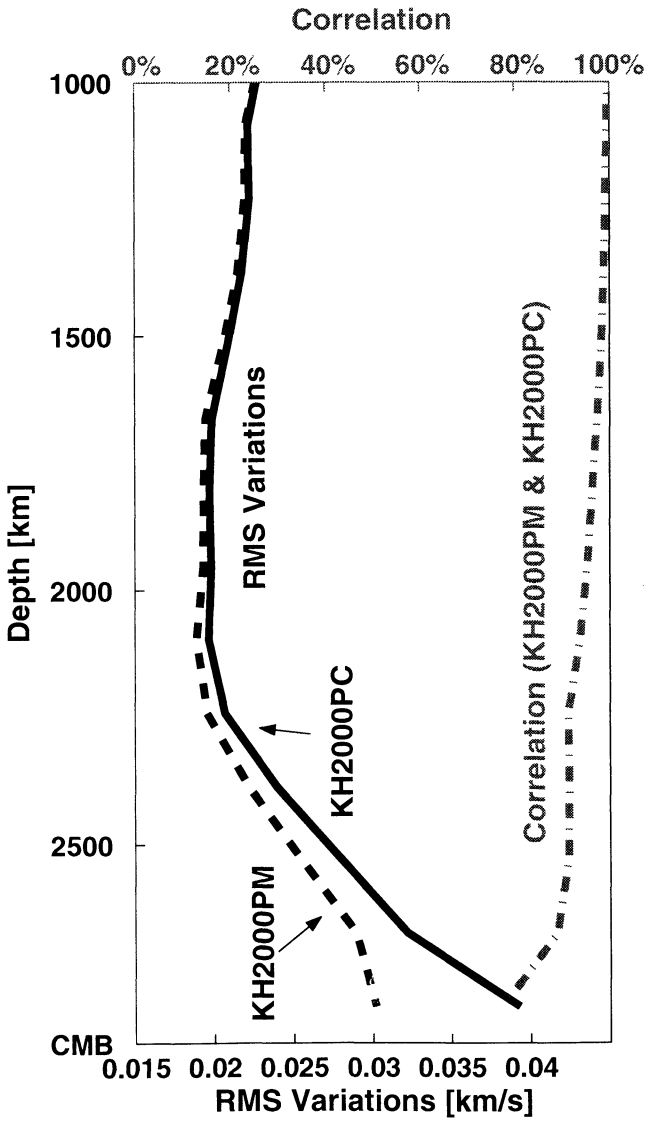


**Figure 7.** The rms value (solid lines) of wave speed amplitudes for models KH2000PM (dashed line) and KH2000PC (unbroken line). Correlation between the models is depicted by the shaded line.

## 5. Trade-off With Core Structure

### 5.1. Inner Core

Differential times involving $PKP_{\mathrm{DF}}$ can map signal from the inner core into the mantle and vice versa. For the results presented in Plate 5 we have corrected the travel times of $PKP_{\mathrm{DF}}$ branch according to a model for inner core anisotropy by *Su and Dziewonski* [1995]. However, there is no consensus on inner core anisotropy and this correction does not account for any isotropic heterogeneity. Therefore, we carried out three test inversions to assess the dependence of our model on inner core structure. In the first we excluded near polar $PKP_{\mathrm{DF}}$ paths since they are most sensitive to axial anisotropy. In the second we simply omitted the correction for inner core anisotropy. In the third we adapted the model parameterization and introduced ~1300 cells in the inner core and allowed them to absorb as much signal in the $PKP_{\mathrm{DF}}$ travel time residuals as they can. The models resulting from tests two and three can be considered as end-member cases regarding the influence of inner core structure on our mantle model results. Comparison with the result discussed above (Plates 3d and 5) shows that in general the pattern of deep mantle structure is, for our set of differential times, virtually independent of our treatment of inner core structure. However, the amplitude of the high wave speed anomalies in the deep mantle beneath Alaska and between South Africa and Antarctica should be interpreted with caution.

### 5.2. Outer Core

*Vasco and Johnson* [1998] suggested the existence of aspherical wave speed variations in the liquid outer core with an rms amplitude of ~50% of that of mantle structure. We investigated the trade-off between mantle and outer core structure with a series of test inversions and discuss the result by means of radial profiles of rms wave speed perturbations (Figure 8).

First, we adapted the parameterization (see section 3.2) and inverted our data set for aspherical structure in both the mantle and the outer core. Figure 8 (shaded circles) suggests that the data allow significant rms variations in the liquid outer core, albeit at lower amplitudes than in the mantle, which is consistent with *Vasco and Johnson* [1998]. Comparison with the result from inversion for mantle structure only (open circles, Figure 8) suggests that the trade-off con-

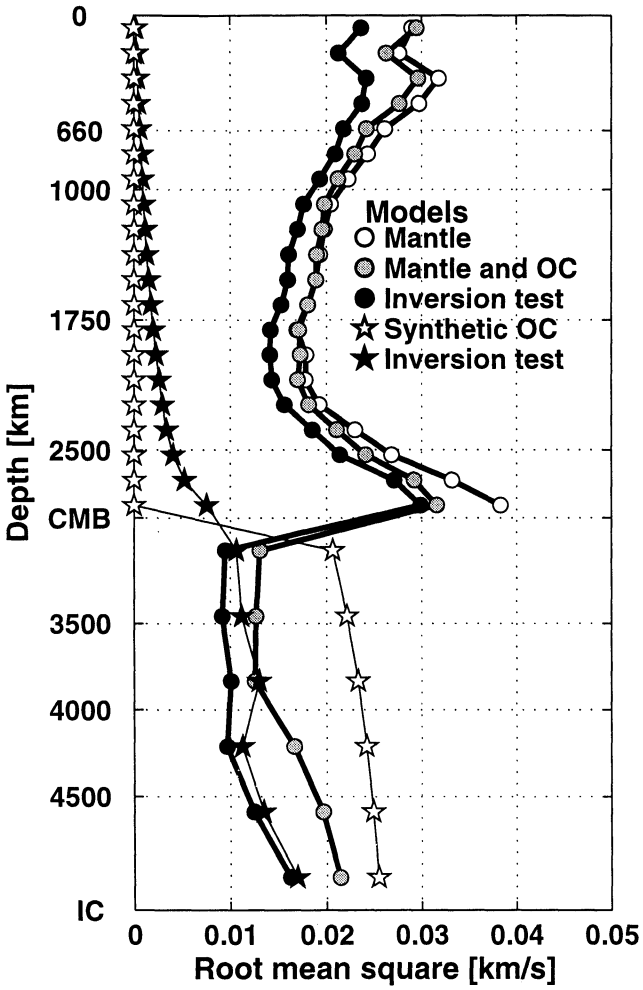


**Figure 8.** The rms of wave speed variations within each layer for models based on EHB98 $P+$ and both $PKP$ data sets. Open circles indicate model confined to the mantle. Shaded circles indicate model of mantle and outer core. Solid circles indicate recovery of inversion test using the model confined to the mantle as an input. Open stars indicate synthetic structure with $\pm 1\%$ wave speed variations on $30° \times 30°$ cells within the outer core. Solid stars indicate recovery of synthetic outer core structure.

cerns the strong heterogeneity in the mantle beneath 2300 km and, surprisingly, above 1000 km depth.

Second, we inverted synthetic data calculated using our model KH2000PC (i.e., no wave speed perturbations in the outer core) for both mantle and core structure. No minimization of the radial component of the gradient across the CMB was applied. Figure 8 (solid dots) demonstrates that potentially the mapping of mantle structure into the outer core is significant. Apart from a slight drop in amplitude, which is typical in such tests, the resulting radial rms profile is rather similar to the one obtained from the inversion of all original data (shaded circles). This suggests that the structure inferred from tomographic inversion of $P$ and $PKP$ data (Figure 8, shaded circles) can be explained by contamination of mantle structure and that outer core structure itself may not contribute much, if anything, to the structural signal in the $PKP$ data used in our study.

Third, we inverted synthetic data calculated for a model with structure in the outer core only (Figure 8, open stars). In this case, the mantle structure is set to zero so that all synthetic $P$ data are zero, which results in a very significant bias to small amplitude in the inversion result. Despite this severe condition, some outer core structure leaks to lower mantle depths (Figure 8, solid stars), presumably along $PKP$ branches that sample regions devoid of EHB98 $P+$ paths. However, even if we take the rms of core structure comparable to that of the lower mantle the rms of the deep mantle artifacts is almost 1 order of magnitude less than the lateral variations inferred from the real data (Plate 5).

## 6. Summary and Conclusions

We have improved the constraints on variations in lower mantle $P$ wave speed by incorporating $PKP$ and $P_{\text{diff}}$ travel time information. These phases sample the deep mantle in a different way than the $P$ phases used in our previous global inversions, and resolution tests suggest that addition of these phases slightly improves the images of structure in the deep mantle. However, integrating data sets that differ substantially in size, quality, and frequency content is neither trivial nor unique. The integration of the different data was guided by the improvement of data fit for all data involved. We have inverted the high-quality differential travel time residuals for $PKP$ and $P_{\text{diff}}$ phases and also used them as the reference for the reduction of the $PKP$ residuals from the data set by *Engdahl et al.* [1998]. The long period $PKP_{\text{DF}}$-$P_{\text{diff}}$ data have large Fresnel zones, and back projection of the data along infinitesimally narrow ray paths is not appropriate. To account for finite frequency effects we have developed a technique to calculate realistic estimates of 3-D sensitivity kernels, based on exact Fréchet kernels calculated by L. Zhao (personal communication, 1999) using normal mode summation with consideration of cross-branch mode coupling [*Zhao and Jordan*, 1998; *Zhao et al.*, 2000]. The use of these kernels allows us to properly distribute the sensitivity for a given seismic phase over a large mantle volume while allowing the high-frequency data to constrain small-scale structure. Finally, we investigated the trade-off between mantle and core structure and the possible contamination of our mantle model with signal pertaining to inner core anisotropy. From these investigations we reach the following conclusions:

1. The inversion of the core phases along with the short period $P$, $pP$, and $pwP$ data resulted in an aspherical model for compressional wave speed that explains a large fraction of the structural signal in the core phases without degrading the fit to the other data used.

2. On the basis of the improved data fit and results of our resolution tests, we conclude that the new data have enhanced the lower mantle part of our model. In particular beneath the Southern Hemisphere the amplitude of the wave speed perturbations has increased by a factor of 2 and the spatial definition of the wave speed anomalies improved.

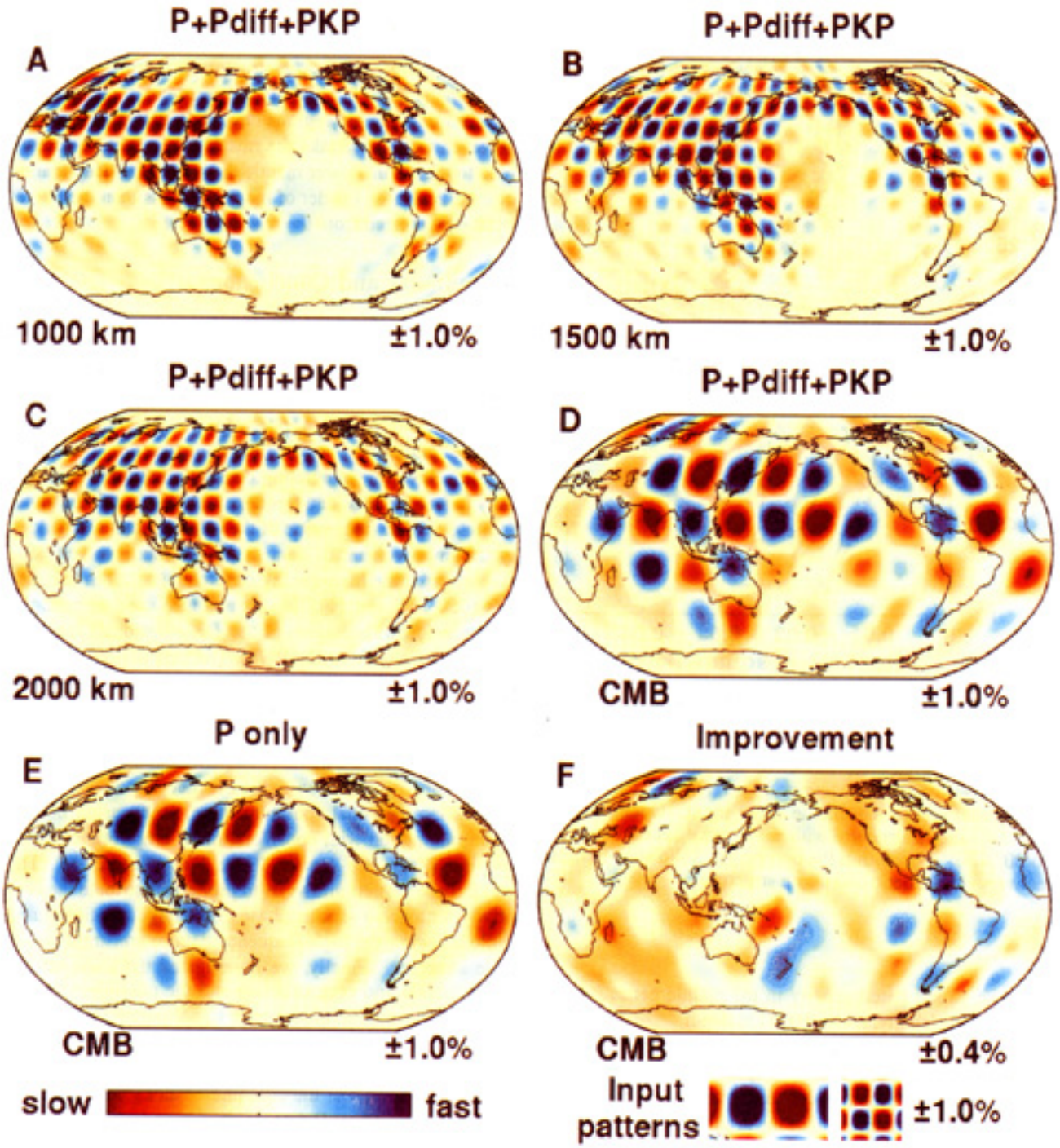


**Plate 4.** Inversion tests using harmonic input patterns with peek values ±2% (see scale bar and input patterns). Recoveries are shown for different data sets. (a)-(d) Same data sets and damping as used for model KH2000PC. (e) Same data sets and damping as used for model KH2000PM. (f) Improvement at the CMB, i.e., the difference between the two recoveries in Plates 4d and 4e.

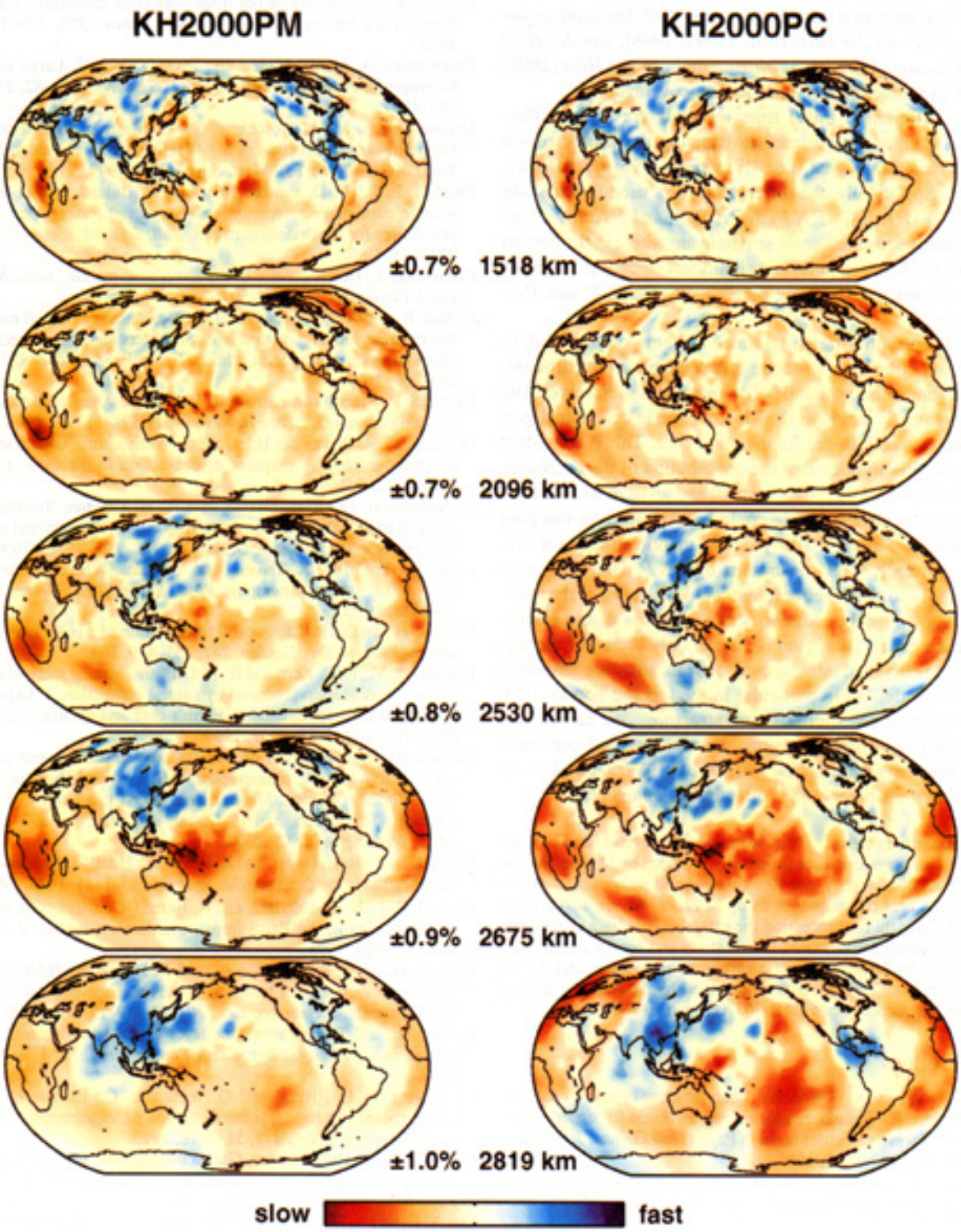


**Plate 5.** Selected layers from model based only on EHB98 $P+$ (KH2000PM) and the final model based on all data (KH2000PC).

However, many features in the "old" models have proved to be robust. Our tests reveal that spatial resolution does not change much from the middle to the lowermost mantle which suggests that the transition near 2000 km depth as described by *van der Hilst et al.* [1997, 1998]; *van der Hilst and Kárason* [1999], and *Kárason and van der Hilst* [2000] is not an artifact of variations in data coverage.

3. Differential travel time residuals are not as effective as commonly assumed in isolating the source region of the structural signal [i.e., *Wysession*, 1996; *Castle et al.*, 2000]. Specifically, the differential pairs used in our study ($PKP_{AB}$-$PKP_{DF}$, $PKP_{AB}$-$PKP_{BC}$, and $PKP_{DF}$-$P_{diff}$) are sensitive to small-scale structure anywhere in the bottom half of the lower mantle, and significant smearing can occur in the lower mantle along the subvertical $PKP$ and $P_{diff}$ paths.

4. Even with differential times it seems very difficult to constrain outer core structure independent of the (stronger) heterogeneity in the mantle. Test inversions of observed data or of synthetic residuals that do not contain core signal give similar rms amplitudes for the outer core. This is consistent with the presumption that the contribution of the outer core to signal in the $PKP$ data is small and all or most of the apparent outer core structure could be explained by mapping ("smearing") along $PKP$ paths of mantle structure that is not sufficiently well constrained by the $P$ data. This may also apply to the inner core but we did not test that explicitly. The strong heterogeneity near the base of the mantle, in the so called D" region is not the only source of the signal that is mapped into the core. Indeed, structure anywhere in the mantle, but in particular in the top and bottom 1000 km, can produce spurious core structure. We cannot rule out outer core heterogeneities, but our data are consistent with the conventional view [*Stevenson*, 1987; *Jellinek et. al*, 1999] that the outer core is effectively homogeneous.

**Acknowledgments.** This work would not have been possible without the waveform data generously provided by Michael Wysession, Tom McSweeney, and Ken Creager, and without the 3-D sensitivity kernels calculated for us by Li Zhao. We are also grateful to E.R. Engdahl for processing the extended data base of routinely reported phase arrivals used in this study and for the constructive comments by Jeroen Ritsema, an anonymous reviewer, and the Associate Editor. This research is supported by the National Science Foundation under grants EAR-9627087 and EAR-9969492.

## References

Abers, G. A., and S. W. Roecker, Deep-structure of an arc-continent collision: Earthquake relocation and inversion for upper mantle P and S wave velocities beneath Papua New Guinea, *J. Geophys. Res.*, *96*, 6379–6401, 1991.

Albarède, F., and R. D. van der Hilst, New mantle convection model may reconcile conflicting evidence, *Eos Trans. AGU*, *80*, 535–539, 1999.

Bijwaard, H., W. Spakman, and E. R. Engdahl, Closing the gap between regional and global travel time tomography, *J. Geophys. Res.*, *103*, 30,055–30,078, 1998.

Boschi, L., and A. M. Dziewonski, High- and low-resolution images of the Earth's mantle: Implications of different approaches to tomographic modeling, *J. Geophys. Res.*, *104*, 25,567–25,594, 1999.

Castle, J., K. C. Creager, J. P. Winchester, and R. D. van der Hilst, Shear wave speeds at the base of the mantle, *J. Geophys. Res.*, *105*, 21,543–21,557, 2000.

Creager, K., Anisotropy of the inner core from differential travel times of the phases *PKP* and *PKIKP*, *Nature*, *356*, 309–314, 1992.

Dziewonski, A. M., B. Hager, and R. J. O'Connell, Large scale heterogeneities in the lower mantle, *J. Geophys. Res.*, *82*, 239–255, 1977.

Dziewonski, A. M., L. Boschi, Y. Gu, G. Master, and G. Laske, Feasibility of construction of a 3-D reference Earth model, *Eos Trans. AGU 80*(46), Fall Meet. Suppl., F24, 1999.

Engdahl, E. R., R. D. van der Hilst, and R. Buland, Global teleseismic earthquake relocation with improved travel times and procedures for depth determination, *Bull. Seismol. Soc. Am.*, *88*, 722–743, 1998.

Garnero, E. J., Heterogeneity of the lowermost mantle, *Annu. Rev. Earth Planet. Sci.*, *28*, 477–507, 2000.

Gilbert, F., and A. M. Dziewonski, An application of normal mode theory to the retrieval of structure parameters and source mechanisms from seismic spectra, *Philos. Trans. R. Soc. London*, *278*, 187–269, 1975.

Grand, S. P., Mantle shear structure beneath the Americas and surrounding oceans, *J. Geophys. Res.*, *99*, 11,591–11,621, 1994.

Grand, S. P., R. D. van der Hilst, and S. Widiyantoro, Global seismic tomography: A snapshot of convection in the earth, *GSA Today*, *7*, 1–7, 1997.

Gudmundsson, O., J. H. Davies, and R. W. Clayton, Stochastic analysis of global traveltime data: Mantle heterogeneity and random errors in the ISC data, *Geophys. J. Int.*, *102*, 25–43, 1990.

Inoue, H., Y. Fukao, K. Tanabe, and Y. Ogata, Whole mantle P-wave travel time tomography, *Phys. Earth Planet. Inter.*, *59*, 294–328, 1990.

Jeffreys, H., and E. R. Lapwood, The reflection of a pulse within a sphere, *Proc. R. Soc. London*, *241*, 455–479, 1957.

Jellinek, A. M., R. C. Kerr, and R. W. Griffiths, Mixing and compositional stratification produced by natural convection, 1. Experiments and their application to Earth's core and mantle, *J. Geophys. Res.*, *104*, 7183–7201, 1999.

Kárason, H., and R. D. van der Hilst, Constraints on mantle convection from seismic tomography, in *History and Dynamics of Plate Motion, Geophys. Monogr. Ser.,* vol. 121, edited by M. A. Richards, R. Gordon, and R. D. van der Hilst, pp. 277–288, AGU, Washington, D.C., 2000.

Kellogg, L. H., B. H. Hager, and R. D. van der Hilst, Compositional stratification in the deep mantle, *Science*, *283*, 1881–1884, 1999.

Kennett, B. L. N., E. Engdahl, and R. Buland, Constraints on seismic velocities in the Earth from traveltimes, *Geophys. J. Int.*, *122*, 108–124, 1995.

Kennett, B. L. N., S. Widiyantoro, and R. D. van der Hilst, Joint seismic tomography for bulk sound and shear wave speed in the Earth's mantle, *J. Geophys. Res.*, *103*, 12,469–12,493, 1998.

Kohler, M., and T. Tanimoto, One-layer global inversion for outermost core velocity, *Phys. Earth Planet. Inter.*, *72*, 173–184, 1992.

Lévêque, J. J., L. Rivera, and G. Wittlinger, On the use of the checkerboard test to assess the resolution of tomographic inversions, *Geophys. J. Int.*, *115*, 313–318, 1993.

Li, C. D., and B. Romanowicz, Global mantle shear velocity model developed using non-linear asymptotic coupling theory, *J. Geophys. Res.*, *101*, 22,245–22,272, 1996.

Liu, X. F., and A. M. Dziewonski, Global analysis of shear wave velocity anomalies in the lower-most mantle, in *The Core-Mantle Boundary Region,* Geodyn. ser. vol. 28, edited by M. Gurnis et al., pp. 21–36, AGU, Washington, D.C., 1998.

Liu, X. F., J. Tromp, and A. M. Dziewonski, Is there a first order discontinuity in the lowermost mantle?, *Earth Planet. Sci. Lett.*, *160*, 343–354, 1998.

Masters, G., G. Laske, and H. Bolton, A shear-velocity model of

the mantle, *Philos. Trans. R. Soc. London, Ser. A*, *354*, 1385–1411, 1996.

McSweeney, T. J., Seismic constraints on core structure and dynamics, Ph.D. thesis, Univ. of Wash., Seattle, 1995.

Mégnin, C., and B. Romanowicz, The three-dimensional shear velocity structure of the mantle from the inversion of body, surface, and higher-mode waveforms, *Geophys. J. Int.*, *143*, 709–728, 2000.

Nolet, G., Solving or resolving inadequate and noisy tomographic systems, *J. Comput. Phys*, *61*, 463–468, 1985.

Nolet, G., Seismic wave propation and seismic tomography, in *Seismic Tomography, With Application, in Global Seismology and Exploration Geophysics*, edited by G. Nolet, pp. 1–27, D. Reidel, Norwell, Mass., 1987.

Nolet, G., R. Montelli, and J. Virieux, Explicit, approximate expressions for the resolution and a posteriori covariance of massive tomographic systems, *Geophys. J. Int.*, *138*, 36–44, 1999.

Paige, C. C., and M. A. Saunders, LSQR: An algorithm for sparse linear equations and sparse least squares, *Trans. Math. Software*, *8*, 43–71, 1982.

Pulliam, R. J., D. W. Vasco, and L. R. Johnson, Tomographic inversions for mantle *P* wave velocity structure based on the minimization of l2 and l1 norms of international seismological center travel time residuals, *J. Geophys. Res.*, *98*, 699–734, 1993.

Ritsema, J., S. Ni, D. V. Helmberger, and H. P. Crotwell, Anomalous shear velocity reductions and gradients in the lower mantle beneath Africa, *Geophys. Res. Lett.*, *25*, 4245–4248, 1998.

Ritsema, J., H. van Heijst, and J. Woodhouse, Complex shear wave velocity structure imaged beneath Africa and Iceland, *Science*, *286*, 1925–1928, 1999.

Robertson, G. S., and J. H. Woodhouse, Evidence for proportionality of *p* and *s* heterogeneity in the lower mantle, *Geophys. J. Int.*, *123*, 85–116, 1995.

Song, X., and D. V. Helmberger, Depth dependance of anistropy of earth's inner core, *J. Geophys. Res.*, *100*, 9805–9816, 1995.

Song, X., and D. V. Helmberger, *PKP* differential travel times: Implications for 3-d lower mantle structure, *Geophys. Res. Lett.*, *24*, 1863–1866, 1997.

Spakman, W., and G. Nolet, Imaging algorithms, accuracy and resolution in delay time tomography, in *Mathematical Geophysics: A Survey of Recent Developments in Seismology and Geodynamics*, edited by N. J. Vlaar, pp. 155–188, D. Reidel, Norwell, Mass., 1988.

Stevenson, D. J., Limits on lateral density and velocity variations in the Earth's outer core, *Geophys. J. R. Astron. Soc.*, *88*, 311–319, 1987.

Su, W. J., and A. M. Dziewonski, On the scale of mantle heteroeneity, *Phys. Earth Planet. Inter.*, *74*, 29–54, 1992.

Su, W. J., and A. M. Dziewonski, Inner core anisotropy in three dimensions, *J. Geophys. Res.*, *100*, 9831–9852, 1995.

Su, W. J., and A. M. Dziewonski, Simultaneous inversion for 3-D variations in shear and bulk velocity in the mantle, *Phys. Earth Planet. Inter.*, *100*, 135–156, 1997.

Su, W. J., R. L. Woodward, and A. M. Dziewonski, Deep origin of mid-oceanic ridge velocity anomalies, *Nature*, *359*, 149–152, 1992.

Su, W. J., R. Woodward, and A. M. Dziewonski, Degree-12 model of shear velocity heterogeneity in the mantle, *J. Geophys. Res.*, *99*, 6945–6980, 1994.

van der Hilst, R. D., and E. R. Engdahl, On ISC *PP* and *pP* data and their use in delay-time tomography of the Caribbean region, *Geophys. J. Int.*, *106*, 169–188, 1991.

van der Hilst, R. D., and H. Kárason, Compositional heterogeneity in the bottom 1000 kilometers of Earth's mantle: Toward a hybrid convection model, *Science*, *283*, 1885–1888, 1999.

van der Hilst, R. D., E. R. Engdahl, and W. Spakman, Tomographic inversion of *P*-data and *pP*-data for aspherical mantle structure below the northwest Pacific region, *Geophys. J. Int.*, *115*, 264–302, 1993.

van der Hilst, R. D., S. Widiyantoro, and E. Engdahl, Evidence for deep mantle circulation from global tomography, *Nature*, *386*, 578–584, 1997.

van der Hilst, R. D., S. Widiyantoro, and K. C. T. J. McSweeney, Deep subduction and aspherical variations in P-wavespeed at the base of Earth's mantle, in *The Core-Mantle Boundary Region, Geodyn. Ser.*, vol. 28, edited by M. Gurnis et al., pp. 5–20, AGU, Washington, D.C., 1998.

van der Sluis, A., and H. A. van der Vorst, Numerical solution of large sparse linear systems arising from tomographic problems, in *Seismic Tomography, With Application in Global Seismology and Exploration Geophysics*, edited by G. Nolet, pp. 53–87, D. Reidel, Norwell, Mass., 1987.

Vasco, D. W., and L. Johnson, Whole earth structure estimated from seismic arrival times, *J. Geophys. Res.*, *103*, 2633–2671, 1998.

Vasco, D. W., R. J. Pulliam, and L. R. Johnson, Formal inversion of ISC arrival times for mantle P-velocity structure, *Geophys. J. Int.*, *113*, 586–606, 1993.

Vasco, D. W., L. R. Johnson, R. J. Pulliam, and P. S. Earle, Robust inversion of iasp91 travel time residuals for mantle P and S velocity structure, earthquake mislocations, and station corrections, *J. Geophys. Res.*, *99*, 13,727–13,755, 1994.

Vasco, D. W., L. R. Johnson, and J. Pulliam, Lateral variations in mantle velocity structure and discontinuities determined from *P*, *PP*, *S*, *SS*, and *SS-SdS* travel time residuals, *J. Geophys. Res.*, *100*, 24,037–24,059, 1995a.

Vasco, D. W., J. E. Peterson, and E. L. Majer, Beyond ray tomography: Wavepaths and fresnel volumes, *Geophysics*, *60*, 1790–1804, 1995b.

Vasco, D. W., L. R. Johnson, and O. Marques, Global earth structure: inference and assassment, *Geophys. J. Int.*, *137*, 381–407, 1999.

Widiyantoro, S., Studies of seismic tomography on regional and global scale, Ph.D. thesis, 256 pp., Aust. Nat. Univ., Canberrra, 1997.

Woodhouse, J. H., and A. M. Dziewonski, Seismic modeling of the Earth's large-scale 3-dimensional structure, *Philos. Trans. R. Soc. London*, *328*, 291–308, 1989.

Woodward, R. L., and G. Masters, Global upper mantle structure from long-period differential travel times, *J. Geophys. Res.*, *96*, 6351–6377, 1991.

Wysession, M. E., Large-scale structure at the core-mantle boundary from diffracted waves, *Nature*, *382*, 244–248, 1996.

Wysession, M. E., R. W. Valenzuela, A. N. Zhu, and L. Barko, Investigating the base of the mantle using differential travel times, *Phys. Earth Planet. Inter.*, *92*, 67–84, 1995.

Zhao, L., and T. H. Jordan, Sensitivity of frequency-dependent traveltimes to laterally heterogenous, anisotropic earth structure, *Geophys. J. Int.*, *133*, 683–704, 1998.

Zhao, L., T. H. Jordan, and C. H. Chapman, Three-dimensional Frèchet differential kernels for the seismic delay times, *Geophys. J. Int.*, *141*, 558–576, 2000.

H. Kárason and R. D. van der Hilst, Department of Earth, Atmospheric and Planetary Sciences, Massachusetts Institute of Technology, Room 54-517A, Cambridge, MA 02139-4307. (karason@mit.edu; hilst@mit.edu)

(Received July 22, 1999; revised October 12, 2000;
accepted October 24, 2000.)